ADVANCED FUNCTIONAL MATERIALS

Supporting Information

for *Adv. Funct. Mater.*, DOI: 10.1002/adfm.202004312

Charge-Carrier Trapping and Radiative Recombination in Metal Halide Perovskite Semiconductors

*Michael J. Trimpl, Adam D. Wright, Kelly Schutt, Leonardo R. V. Buizza, Zhiping Wang, Michael B. Johnston, Henry J. Snaith, Peter Müller-Buschbaum, and Laura M. Herz**

Supporting Information: Charge-Carrier Trapping and Radiative Recombination in Metal Halide Perovskite Semiconductors

Michael J. Trimpl,[†,‡] Adam D. Wright,[†] Kelly Schutt,[†] Leonardo Buizza,[†] Zhiping Wang,[†] Michael B. Johnston,[†] Henry J. Snaith,[†] Peter Müller-Buschbaum,[‡,¶] and Laura M. Herz[*,†]

†*Department of Physics, University of Oxford, Clarendon Laboratory, Parks Road, Oxford OX1 3PU, United Kingdom*

‡*Technische Universitt München, Physik Department, Lehrstuhl fr Funktionelle Materialien, James-Franck-Str. 1, 85748 Garching, Germany*

¶*Heinz Maier-Leibnitz-Zentrum, Lichtenbergstr. 1, 85748 Garching, Germany*

E-mail: laura.herz@physics.ox.ac.uk

Contents

1 Sample fabrication

In the main article, we report the charge-carrier dynamics of a thin film of $FA_{0.95}Cs_{0.05}PbI_3$. Additionally, we analyzed a thin film of $FA_{0.83}Cs_{0.17}PbI_3$ fabricated by a different researcher. We chose samples with distinct material composition that were fabricated by different researchers to ensure that the observed dynamics, including rapid initial PL transients and the temperature dependent decay rates, are general to this material group. We focus on a similar material composition of $FA_{1-x}Cs_xPbI_3$ that has exhibited promising crystal quality in recent work. A cesium content of $x = 0.1$ in $FA_{1-x}Cs_xPbI_3$ has shown to result in a decrease in trap density and an enhancement of the power conversion efficiency in solar cell devices[S1] Furthermore, a cesium content ranging from $x = 0.1$ to $x = 0.30$ has shown improved material properties for MA- and FA-based MHPs, as well as mixed-halide and mixed-cation MHPs.[S1-S5] Both samples show similar PL transient decays. In the following sections, XRD and PL measurements of $FA_{0.83}Cs_{0.17}PbI_3$ thin films are included alongside those for $FA_{0.95}Cs_{0.05}PbI_3$ thin film for comparison. Preparation methods for both films are as follows:

1.1 $FA_{0.95}Cs_{0.05}PbI_3$

Spin-coated perovskite thin film. 1.45 M $FA_{0.95}Cs_{0.05}PbI_3$ solution perovskite precursor solution was prepared using a 4 : 1 (volume:volume) mixed solvent from anhydrous DMF (Sigma-Aldrich) and DMSO (Sigma-Aldrich). The precursor salts used were formamidinium iodide (FAI; Dyesol), cesium iodide (CsI; Alfa Aesar), lead iodide (PbI_2; TCI), and methylammonium chloride (MACl; Dyesol). The composition of FA, Cs and Pb, was mixed in solution at the molar ratios of 0.95:0.05:1.0, respectively. As a processing additive 0.05 excess of MACl, with respect to the lead, was added to the solution. The solution was prepared in a nitrogen-filled glovebox and kept stirring overnight at room temperature. The precursor

solution was spin-coated through a two-step spin coating program in a drybox with relative humidity below 20% (10 s at 1000 rpm and 35 s at 6000 rpm). Anisole (Sigma-Aldrich) was dripped during the second step as an antisolvent, 10 s before the end. The films were then annealed at 100 °C for 60 min. Most of the volatile MACl is driven off during the curing process. This has a very positive influence upon the smooth appearance and optoelectronic properties of the crystalized films.

1.2 $FA_{0.83}Cs_{0.17}PbI_3$

Spin-coated perovskite thin film. A 1.45 M stoichiometric perovskite precursor solution for $FA_{0.83}Cs_{0.17}PbI_3$ was prepared immediately prior to thin film deposition. Cesium iodide (CsI; Alfa Aesar, 64 mg), formamidinium iodide (FAI; Dyesol, 207 mg), and lead iodide (PbI_2; TCI Chemicals, 668 mg) were dissolved in 800 μL DMF and 200 μL DMSO in ambient conditions. The precursor was then vigorously stirred for 15 minutes at 70°C, and allowed to cool to room temperature before spin coating. The solution was spin coated in a dry box (relative humidity $< 20\%$) at 1000 rpm for 10 seconds followed by 6000 rpm for 35 seconds. 10 seconds before the end of spin coating, 100 μL anisole was quickly dropped onto the substrate. The films were annealed at 100°C for 15 minutes. The films were visibly smooth and uniform with specular reflections, and no MACl additive was used.

2 XRD measurements

In this section the XRD spectra of a $FA_{0.95}Cs_{0.05}PbI_3$ and a $FA_{0.83}Cs_{0.17}PbI_3$ thin film are shown. While $FA_{0.95}Cs_{0.05}PbI_3$ is discussed in detailed in the main article, we chose to analyze also $FA_{0.83}Cs_{0.17}PbI_3$ to confirm the discussed dynamics are also applicable to similar materials. Both samples show similar PL transient decays. The XRD spectra suggest that $FA_{0.95}Cs_{0.05}PbI_3$ has a better crystal quality than $FA_{0.83}Cs_{0.17}PbI_3$ due to higher peak counts, as shown in Figure S1. However, the Bragg peak intensities also depend on the thickness of the sample, the size and the orientation of the crystallites, as well as other structural properties. Therefore, Bragg peak intensities are not unambiguously related to crystal quality. PL measurements for the $FA_{0.83}Cs_{0.17}PbI_3$ film (see Section 4, Figure S5) reveal some sub-band gap PL emission in across a wide temperature range, indicative of slightly increased energetic disorder in the material.

Therefore, we focus our analysis on the higher-quality $FA_{0.95}Cs_{0.05}PbI_3$ thin film.

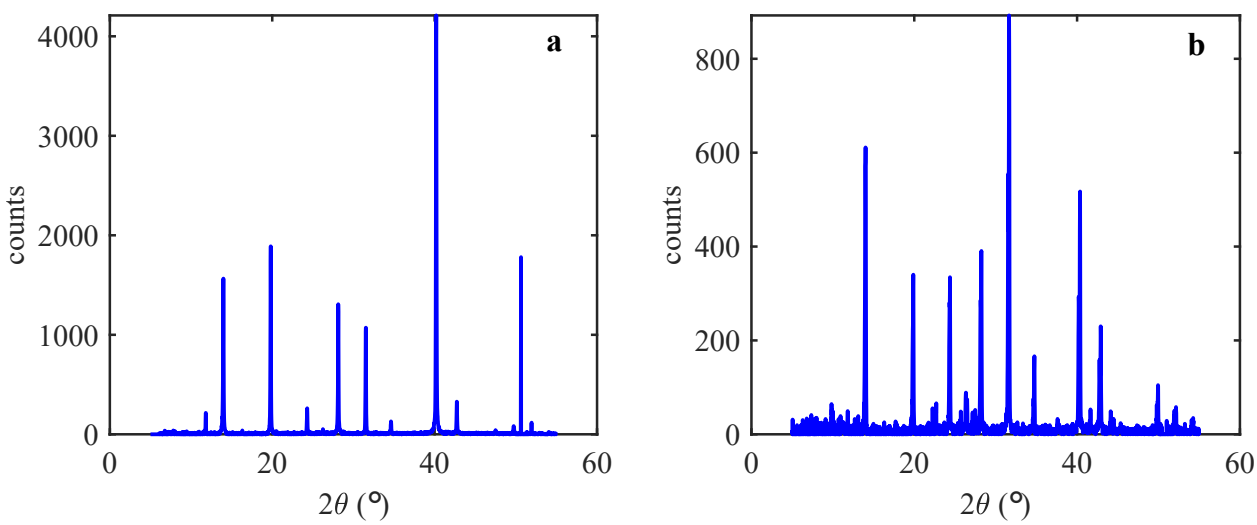

Figure S1: X-ray diffraction spectra of (a) $FA_{0.95}Cs_{0.05}PbI_3$ and (b) $FA_{0.83}Cs_{0.17}PbI_3$ thin-film samples on z-cut quartz substrates taken using a Rigaku Smartlab with a HyPix-3000 detector and a Cu-Source. PbI_2 residues exhibit a Bragg peak at $2\theta = 12.6°$.[S6,S7] Both samples do not exhibit such a Bragg peak at that angle. In (a) we see a peak at $2\theta = 11.8°$, which has been observed in the yellow, hexagonal non-perovskite phase of $FAPbI_3$.[S8] The perovskites Bragg peak positions agree with previous reports.[S8-S11]

3 Absorption spectroscopy and PL spectra

A Fourier transform infrared spectrometer (Bruker Vertex 80v) was used for absorption measurements. A tungsten halogen lamp source, a calcium fluoride beam splitter and silicon detector were used. PL emission occurs just below the band gap in the perovskite thin films (Figure S2). This is indicative of the direct band gap character of perovskite thin-film samples. Experimental details for the PL measurements are found in Section 4. Here, a $FA_{0.95}Cs_{0.05}PbI_3$ and a $FA_{0.83}Cs_{0.17}PbI_3$ thin film are investigated to demonstrate that the dynamics discussed in the main article, referring to $FA_{0.95}Cs_{0.05}PbI_3$, also extend to similar materials.

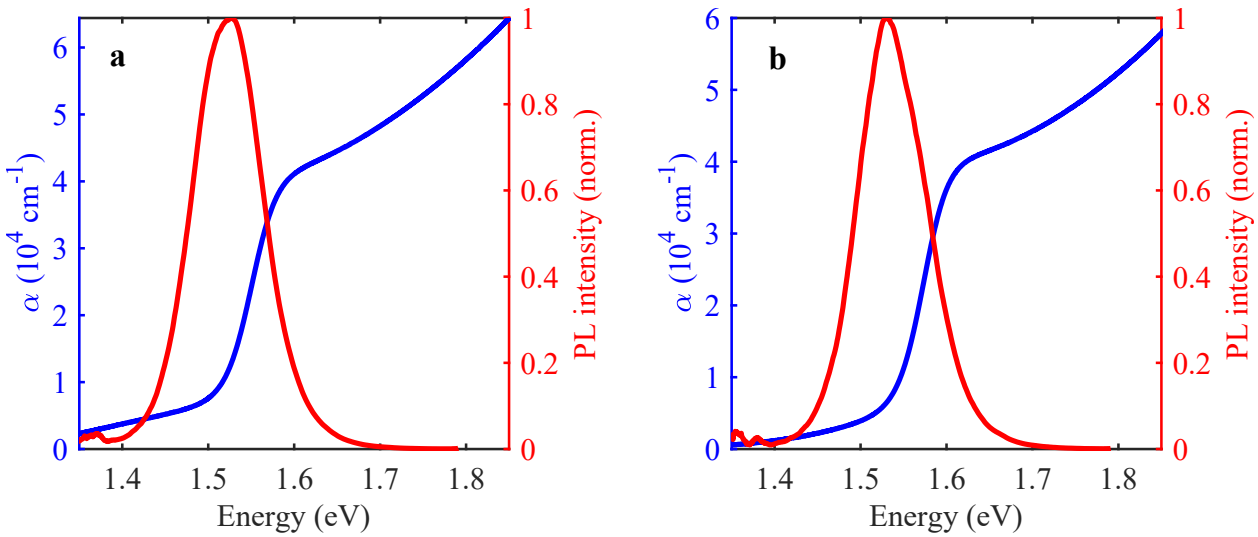

Figure S2: Absorption spectra and PL spectra at room temperature for (a) $FA_{0.95}Cs_{0.05}PbI_3$ ($d = (585 \pm 8)$ nm) and (b) $FA_{0.83}Cs_{0.17}PbI_3$ ($d = (540 \pm 5)$ nm) thin films, with film thickness d and absorption coefficient α. Both samples show PL emission slightly below the absorption edge, typical for direct band gap semiconductors. The absorption spectrum shows a small amount of absorption below the absorption edge that decreases to zero towards lower energies. We attribute this to scattering effects of the samples. The PL spectrum was measured after exciting at an excitation wavelength of $\lambda = 398$ nm at an excitation fluence of $280\,\mathrm{nJ/cm^2}$.

4 Photoluminescence spectra

Samples were photoexcited above bandgap by a 398 nm picosecond pulsed diode laser (PicoHarp, LDH-D-C-405M) with laser pulse frequency set to 1 MHz to match most of the PL transient measurements. The emitted, time-integrated PL was coupled into a grating spectrometer (Princeton Instruments, SP-2558). The spectrally dispersed PL was directed to an iCCD (PI-MAX4, Princeton Instruments).

In this section, we show PL spectra at all measured temperatures for $FA_{0.95}Cs_{0.05}PbI_3$ and $FA_{0.83}Cs_{0.17}PbI_3$ thin films. A comparison of both samples shows that the slightly inferior crystal quality of $FA_{0.83}Cs_{0.17}PbI_3$, as shown in Section 2, reflects in the PL emission. Figure S3 shows a comparison of the temperature dependent PL spectra of $FA_{0.95}Cs_{0.05}PbI_3$ and $FA_{0.83}Cs_{0.17}PbI_3$. Figure S4 and Figure S5 show PL spectra at individual temperatures of $FA_{0.95}Cs_{0.05}PbI_3$ and $FA_{0.83}Cs_{0.17}PbI_3$ thin films respectively. At temperatures above 50 K, the normalized PL spectral shape is independent of fluence in the case of $FA_{0.95}Cs_{0.05}PbI_3$, as shown in Figure S5. In contrast, the PL spectrum of $FA_{0.83}Cs_{0.17}PbI_3$ revealed additional low-energy emission with decreasing excitation fluence at temperatures from 50 K to 200 K. The broadening of the PL spectrum at lower excitation fluence increases up to (150 ± 10) K, near the phase transition. This may be due to changes in band structure and defects due to the strain induced by a higher Cs content.[S12]

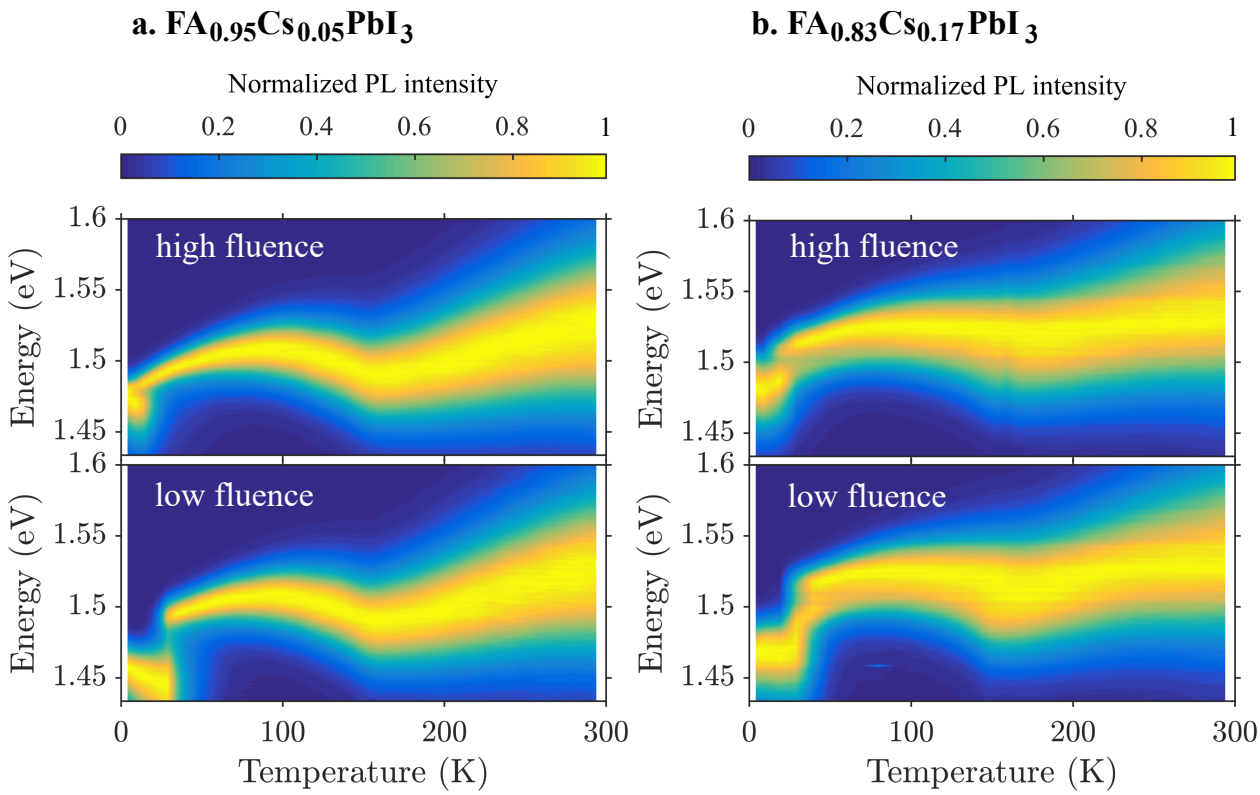

Figure S3: PL spectra of $FA_{0.95}Cs_{0.05}PbI_3$ (left) and $FA_{0.83}Cs_{0.17}PbI_3$ (right) thin films from 4 K to 295 K at two excitation fluences: 3.6 nJ/cm^2 (low fluence), 280 nJ/cm^2 (high fluence) for $FA_{0.95}Cs_{0.05}PbI_3$, and 3.3 nJ/cm^2 (low fluence), 260 nJ/cm^2 (high fluence) for $FA_{0.83}Cs_{0.17}PbI_3$. At temperatures below 50 K, PL emission below the band gap dominates. The emission energy of sub-band-gap states shifts towards lower energy with decreasing excitation fluence.[S13] The spectra broaden with increasing temperature due to electron coupling with longitudinal optical phonons.[S14] A phase transition occurs at 150K.[S15-S17] We observe a broadening of PL emission spectra towards lower excitation fluences in $FA_{0.83}Cs_{0.17}PbI_3$.

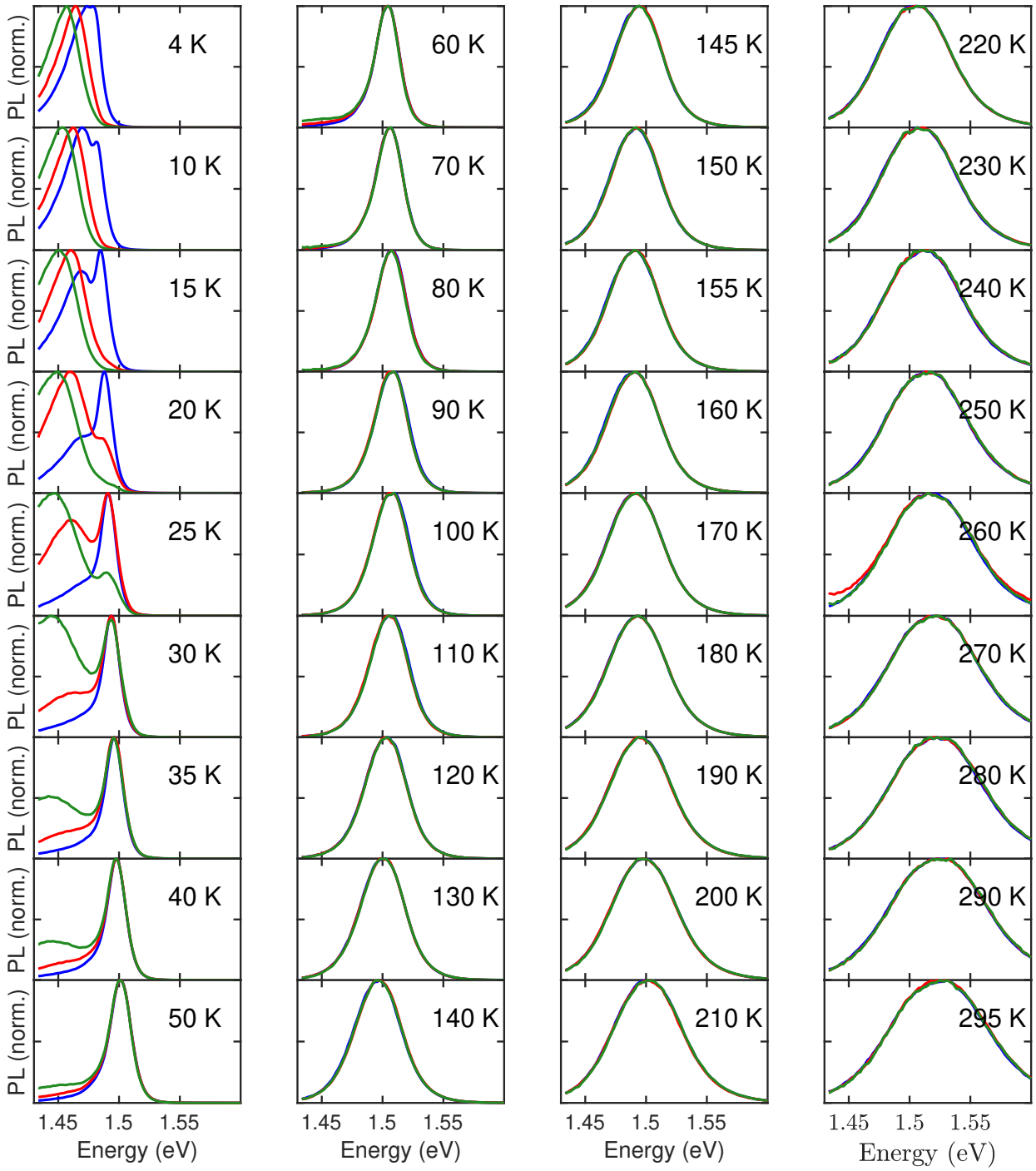

Figure S4: $FA_{0.95}Cs_{0.05}PbI_3$ thin film. Time-integrated PL spectra for sets of three fluences at temperatures from 4 K to 295 K: 3.6 nJ/cm^2 (green), 34 nJ/cm^2 (red), 280 nJ/cm^2 (blue). At low temperatures, the applied excitation fluence changes the emission energy of the sub-band-gap emission. At temperatures above 50K the normalized PL spectrum is independent of excitation fluence.

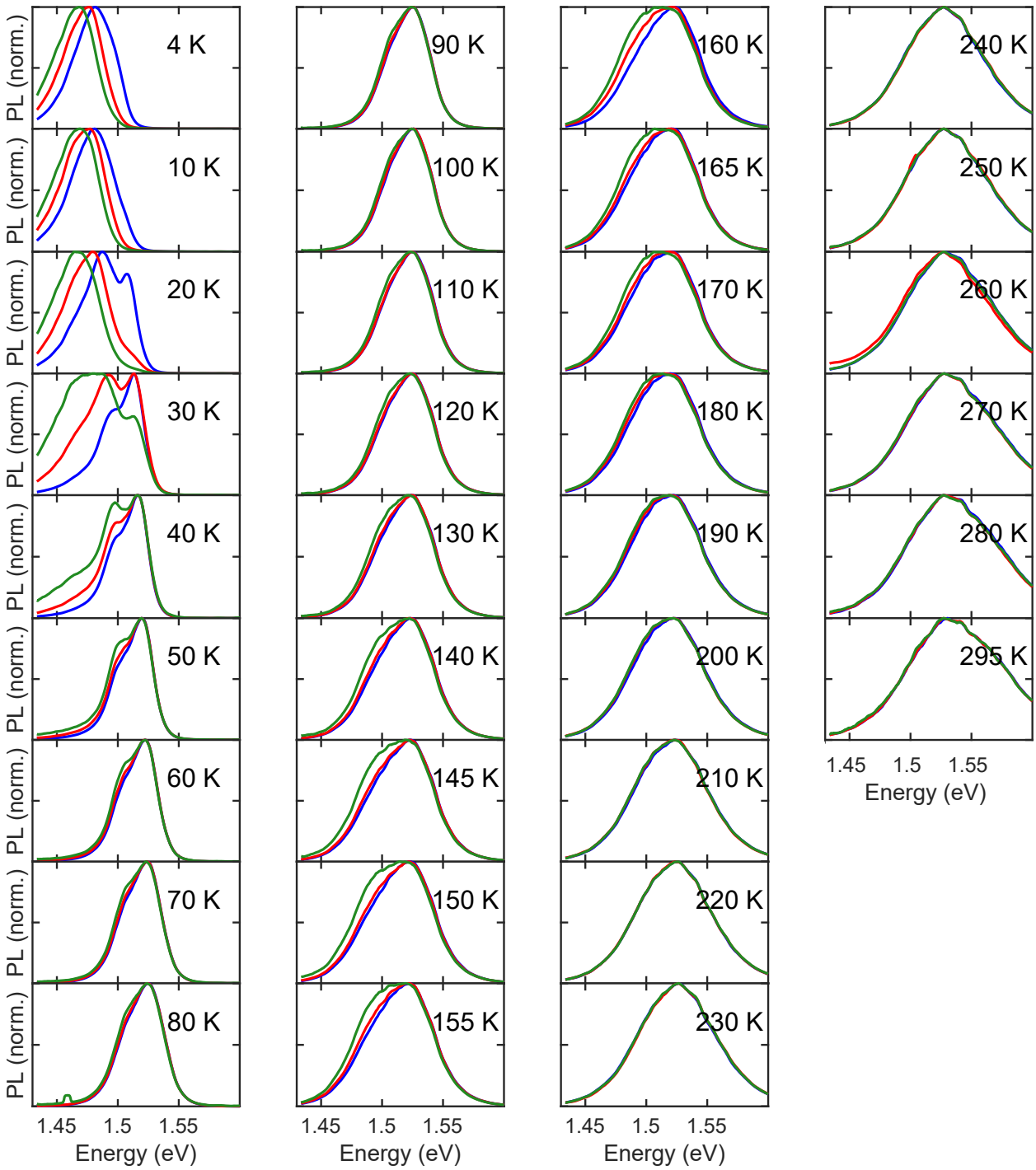

Figure S5: $FA_{0.83}Cs_{0.17}PbI_3$ thin film. Time integrated PL spectra for sets of three fluences at temperatures from 4 K to 295 K: 3.3 nJ/cm^2 (green), 30 nJ/cm^2 (red), 260 nJ/cm^2 (blue). At low temperatures, the applied excitation fluences changes the emission energy of the sub-band-gap emission. For temperatures between 50 K to 180 K additional broadening occurs for the PL emission at low excitation fluence. This may be caused by strain induced by high Cs content.[S12,S18,S19]

5 PLQE

In order to identify the competing radiative and non-radiative recombination mechanisms, we need to determine the photoluminescence quantum efficiency (PLQE) of the perovskite. The PLQE is given by the ratio of radiative recombination to the total recombination rate in the sample. It can hence be used to identify radiative and non-radiative recombination mechanisms.

Experimentally, the PLQE at room temperature can be determined by an integrating sphere or by referencing to a well-known luminescence standard. In the following we discuss the scaling of room-temperature PLQE to lower temperatures; and the suitability of an integrating sphere and a reference standard to determine the PLQE under our experimental conditions.

The PLQE of the employed lead iodide perovskite thin films was measured at room temperature through referencing their radiative efficiency to Rhodamine 6G. At lower temperatures, the external PLQE was obtained by extrapolating from the room temperature measurement through relating their PL emission intensity at each temperature to the value at room temperature.

A relative approach for PLQE measurements has previously been applied by Yong *et al.* on low PLQE samples.[S20] The PLQE of the sample $\mathrm{PLQE_s}$ can be calculated from a known PLQE standard with $\mathrm{PLQE_{ref}}$ by

$$\mathrm{PLQE_s} = \mathrm{PLQE}_{ref} \frac{I_s(\lambda_{\mathrm{PL}})}{I_{\mathrm{ref}}(\lambda_{\mathrm{PL}})} \frac{A_{\mathrm{ref}}(\lambda_{\mathrm{laser}})}{A_{\mathrm{s}}(\lambda_{\mathrm{laser}})} \tag{1}$$

with $I(\lambda_{\mathrm{PL}})$ the integrated emission spectrum and $A(\lambda_{laser})$ the sample absorbance at the excitation wavelength of the laser.[S20]

As a reference, the well-established dilute fluorescence standard Rhodamine 6G was used (PLQE = 95 %).[S21,S22] Rhodamine 6G was chosen as a reference for its exceptionally high PLQE and being a well-established fluorescence standard. Various concentrations of Rho-

damine 6G in ethanol were considered. (15.6 ± 1.0) mg of Rhodamine 6G analytic standard (Sigma Aldrich, molar weight: 479.01 g/mol) were dissolved in 4 ml of Ethanol and subsequently diluted by 1 order of magnitude through multiple steps, resulting in solutions with molar concentrations ranging from 8.3×10^{-3} mol/L (= 3.9 g/L) to 8.3×10^{-6} mol/L (= 0.0039 g/L). The solutions were prepared in a glove box and filled into a 10 mm × 4 mm spectroscopy cuvette from Hellma Analytics. A range of different concentrations were investigated to ensure that the concentrations chosen were low enough to avoid aggregation of the dye. Aggregation would lead to an effective lower Rhodamine 6G concentration in the solvent and potentially suppressed PLQE. Quenching and aggregation have been reported for concentrations higher than 2×10^{-2} mol/l.[S23]

In order to reference the PLQE through Equation 1, the absorption of the samples and Rhodamine 6G is determined using an FTIR spectrometer. Due to the high variation in absorbance, the absorption spectrum of Rhodamine 6G cannot be resolved at all wavelengths. At the laser excitation wavelength of 398 nm, an optical density of 1.2 is obtained for the 0.81 mM solution of Rhodamine 6G in ethanol. The optical density at 398 nm is extrapolated for the other samples. The absorption spectrum at the various concentrations is shown in Figure S6. There is a linear dependence of optical density on Rhodamine concentration across all measured solutions over 3 orders of magnitude of solution concentration (Figure S6 b), confirming the absence of aggregation in the laser dye.

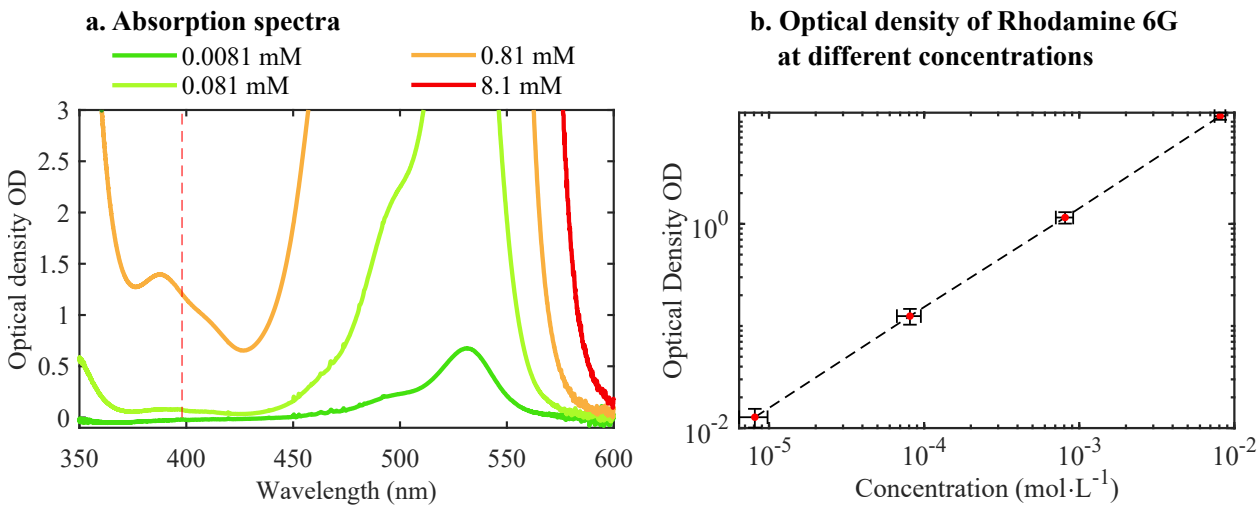

Figure S6: (a) Absorption spectrum of Rhodamine 6G dissolved in ethanol in a 4mm-pathlength cuvette at different concentrations. The red dashed line marks the excitation wavelength for iCCD measurements. (b) Optical density of Rhodamine 6G solutions at different concentrations at the excitation wavelength $\lambda = 398\,\mathrm{nm}$. The correlation between concentration and absorption is linear and aggregation at the measured concentrations is therefore ruled out.

Figure S7 shows that the shape of the PL spectra of Rhodamine 6G is fluence independent, but that the shape of the PL spectra changes slightly with increasing Rhodamine 6G concentration. A red shift of the PL spectra is observed with increasing Rhodamine 6G concentration, which is attributed to self-absorption.

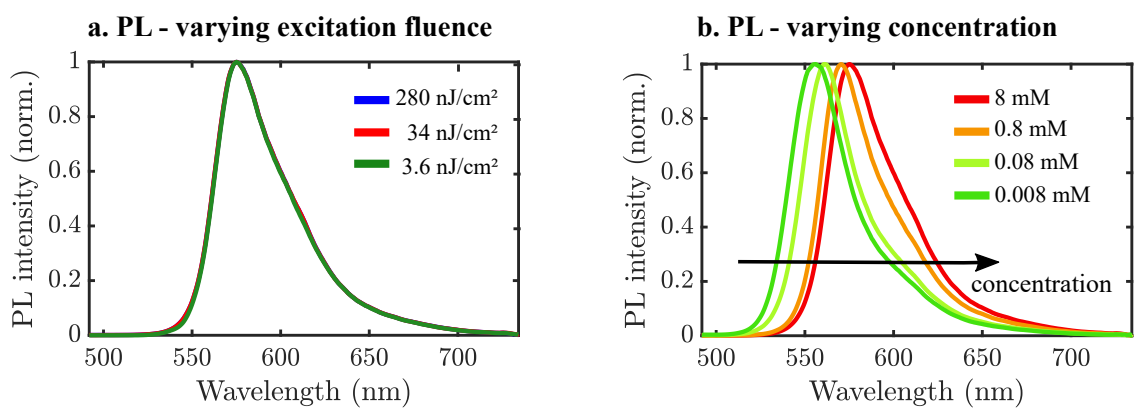

Figure S7: PL emission of Rhodamine 6G in ethanol at different concentrations. (a) PL spectra at different excitation fluences. Excitation fluence has no influence on the shape of PL spectra. (b) PL spectra at different Rhodamine 6G concentrations. Redshift of spectrum with increasing Rhodamine 6G concentration corresponds to higher optical density. The redshift is attributed to self-absorption.

In summary, it has been established that Rhodamine 6G shows no agglomeration in the concentrations employed, and hence, exhibits a PLQE of PLQE = 95 %. Furthermore, analysis of absolute PL intensities showed that the PLQE scales linearly with excitation fluence. The room temperature external PLQE of the perovskite samples was measured by referencing the number of emitted photons between the sample and Rhodamine 6G following Equation 1. The perovskite thin-film sample was mounted in a vacuum cell that was continuously flushed with Helium to reproduce the experimental conditions used in temperature-dependent experiments. In addition, the temperature-dependent external PLQE was determined through a relative scaling of PL measurements across temperature. The temperature-dependent scaling involves only one sample at different temperatures and the total absorption is close to unity $A_{\mathrm{ref}} \approx A_{\mathrm{s}}(T) \approx 1$. Thus, Equation 1 simplifies to

$$\mathrm{PLQE_s} = \mathrm{PLQE}_{ref} \frac{I_s(\lambda_{\mathrm{PL}})}{I_{\mathrm{ref}}(\lambda_{\mathrm{PL}})} \tag{2}$$

The PLQE of $FA_{0.95}Cs_{0.05}PbI_3$ films scaled against Rhodamine 6G at room temperature is shown in Figure S8. The PLQE varies with excitation fluence from PLQE = (0.3 ± 0.2) % (low fluence) to PLQE = (4 ± 1) % (high fluence) at room temperature.

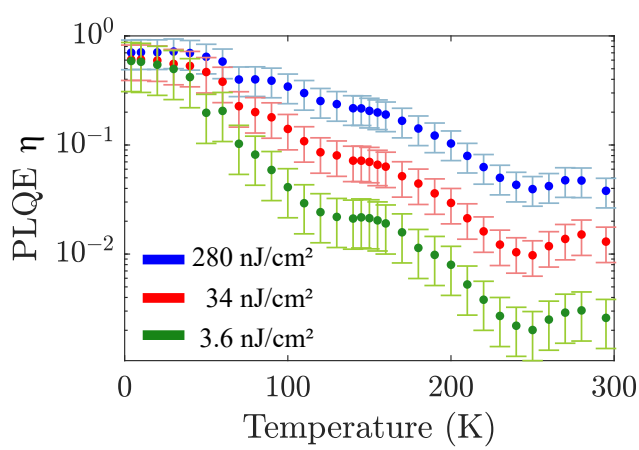

Figure S8: PLQE of $FA_{0.95}Cs_{0.05}PbI_3$ measured at room temperature in respect to Rhodamine 6G. The PLQE across temperature was extrapolated from temperature-dependent PL measurements.

For this work, we chose not to use an integrating sphere for measurements of external

PLQE because the specific experimental conditions employed for PL transients would then not have been reproducible. In addition, Previous studies have suggested that the opto-electronic properties of perovskites are sensitive to atmosphere,[S24–S27] and therefore, it was necessary to measure the external PLQE in Helium atmosphere. Furthermore, an integrating sphere directly compares the laser intensity and photoluminescence in a single measurement. For low PLQE samples, such as the lead iodide thin films studied here, a small error can already largely impact the accuracy in relative terms, particularly at low fluences.

6 Time-resolved photoluminescence

Charge-carrier dynamics were investigated using time-resolved PL measurements based on the time-correlated single photon counting (TCSPC) technique. Samples were photoexcited above bandgap by a 398 nm picosecond pulsed diode laser (PicoHarp, LDH-D-C-405M) with a repetition rate of 1 MHz unless otherwise stated. The emitted PL was coupled into a grating spectrometer (Princeton Instruments, SP-2558). The spectrally dispersed PL was directed to a photon-counting detector (PDM series from MPD). The timing of the photon-counting detector was controlled with a PicoHarp300 TCSPC event timer.

The time-resolved PL was measured over a temperature scale from 4 K to 295 K using a helium-cooled gas exchange cryostat (Oxford Instruments, Optistat CF2) at excitation fluences of 280 nJ/cm^2, 34 nJ/cm^2, 3.6 nJ/cm^2. Figure S9 and Figure S10 show the PL transients at different temperatures for three excitation fluences for a $FA_{0.95}Cs_{0.05}PbI_3$ and $FA_{0.83}Cs_{0.17}PbI_3$ thin film, respectively. In the main article we focused on the $FA_{0.95}Cs_{0.05}PbI_3$ thin film, but here we demonstrate that highly similar dynamics are observed within the same material group. The PL transients at a given fluence, but grouped across temperatures from 50 K to 295 K, are shown in Figure S11 for the $FA_{0.95}Cs_{0.05}PbI_3$ thin film.

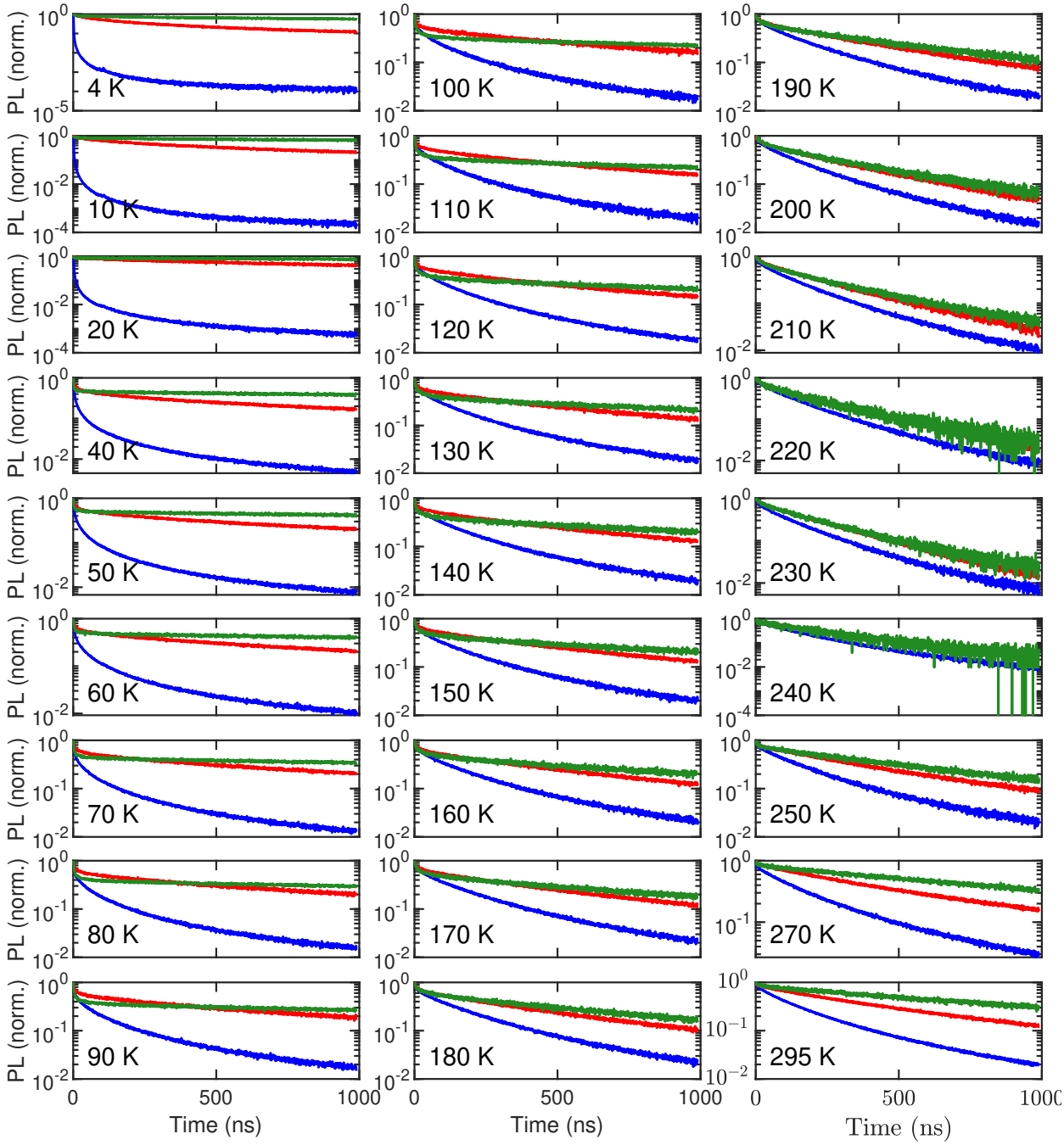

Figure S9: $FA_{0.95}Cs_{0.05}PbI_3$ thin film. Time-resolved PL from 4 K to 295 K at various fluences. The sample was photoexcited at 398 nm at a fluence of 3.6 nJ/cm^2 (green), 34 nJ/cm^2 (red) or 280 nJ/cm^2 (blue). PL was detected at its peak emission wavelength.

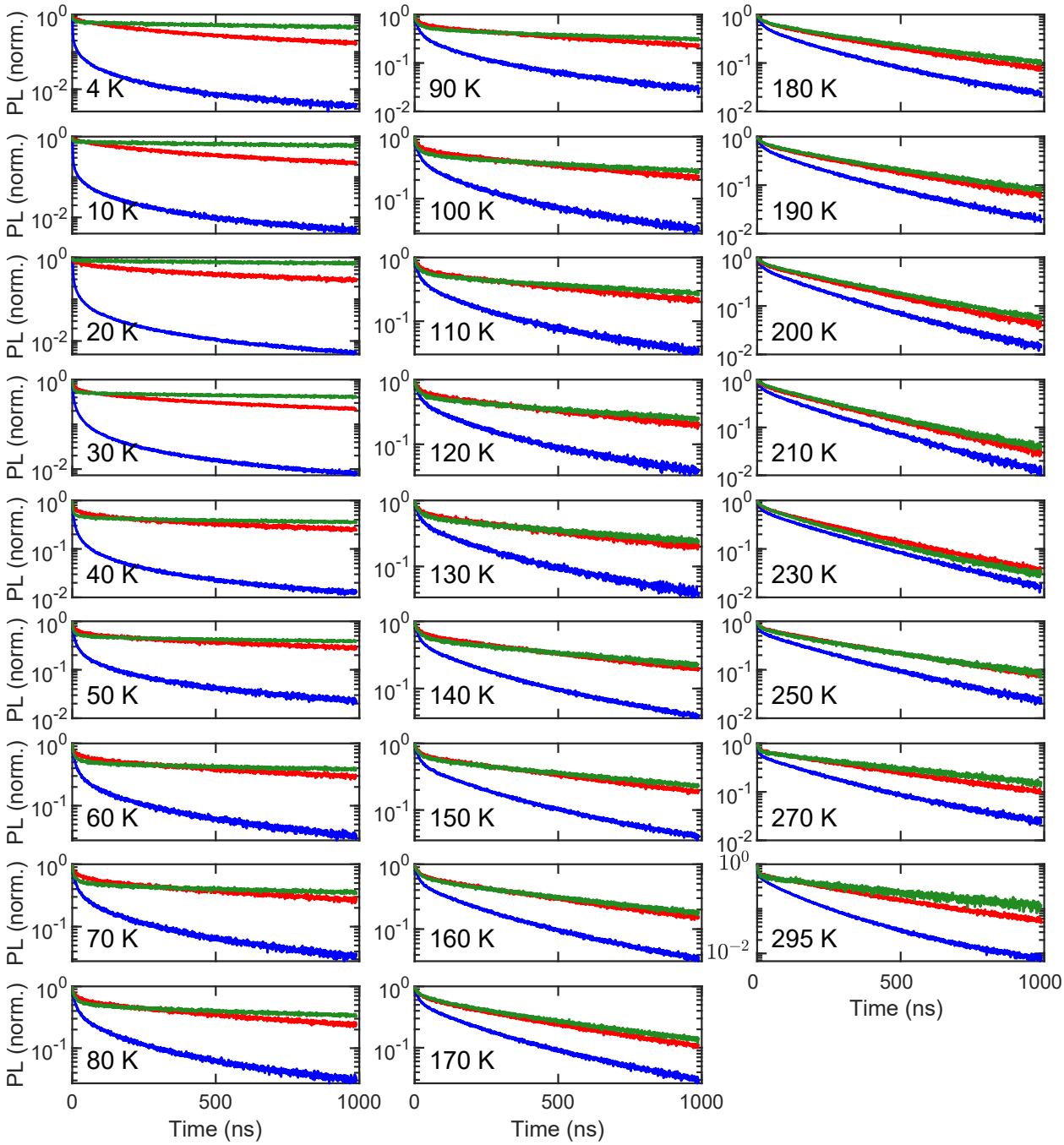

Figure S10: $FA_{0.83}Cs_{0.17}PbI_3$ thin film. Time-resolved PL from 4 K to 295 K at various fluences. The sample was photoexcited at 398 nm at a fluence of 3.3 nJ/cm^2 (green), 30 nJ/cm^2 (red) or 260 nJ/cm^2 (blue). PL was detected at its peak emission wavelength.

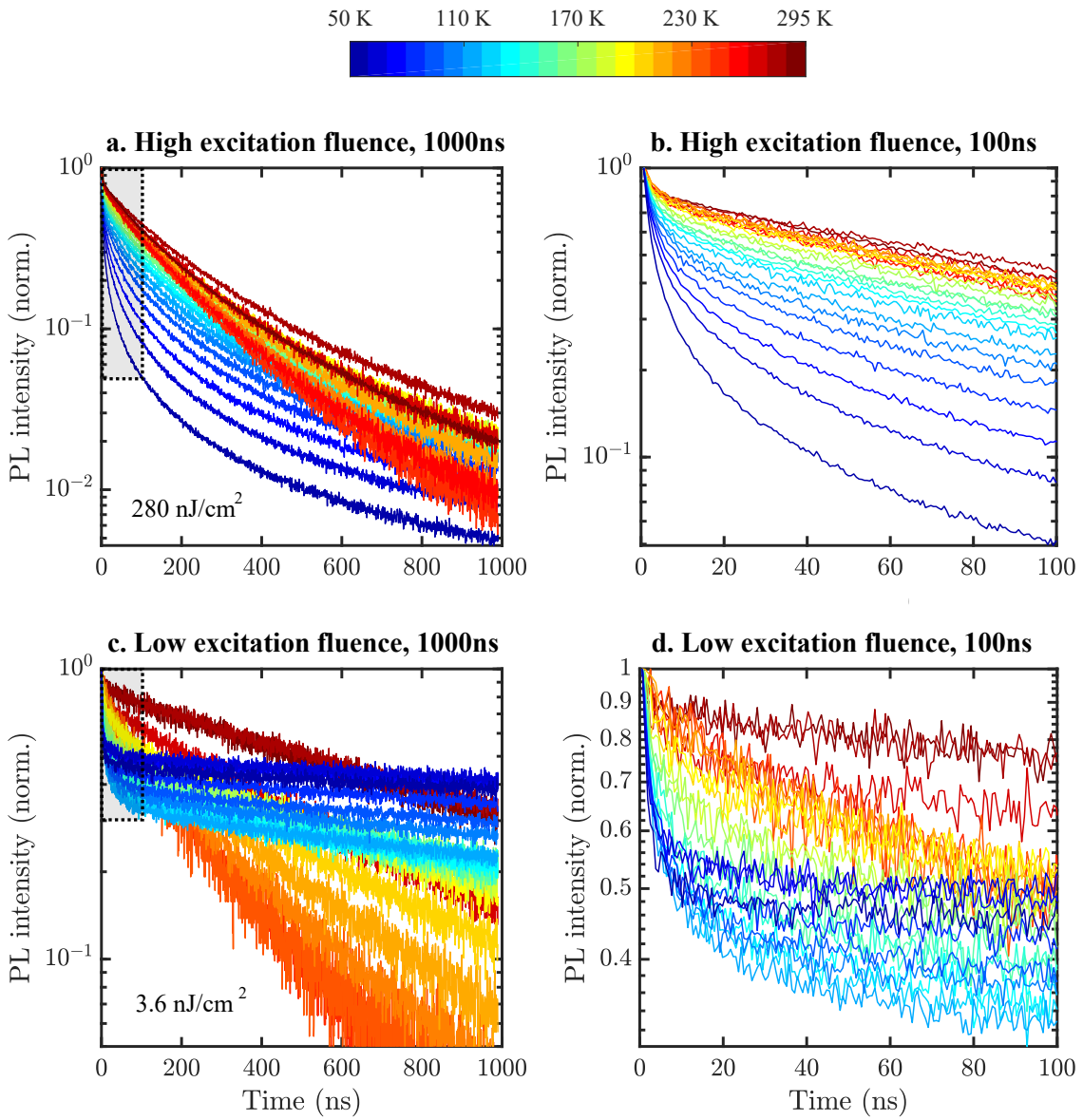

Figure S11: $FA_{0.95}Cs_{0.05}PbI_3$ thin film. Temperature dependence of PL transients at high, 280 nJ/cm^2 (a, b), and low, 3.6 nJ/cm^2(c, d) excitation fluence at temperatures ranging from 50 K to 295 K. The total decay between two consecutive laser pulses is shown on the left at an excitation pulse frequency of 1 MHz. The framed inset indicates the time scale of the corresponding figure (b, d) on the right. Figure (d) shows a fast decay component in the low excitation fluence PL transient measurements that increases in magnitude towards lower temperatures, while the lifetimes after the initial rapid PL decay increase with decreasing temperature.

7 Trap-mediated recombination model

In the main text, we discuss the model illustrated in Figure S12 and described by a set of rate equation, given by:

$$\frac{\mathrm{d}n_\mathrm{e}}{\mathrm{d}t} = -R_\mathrm{pop}(N_\mathrm{T} - n_\mathrm{T})n_\mathrm{e} + R_\mathrm{detrap}n_\mathrm{T} - R_\mathrm{eh}n_\mathrm{e}n_\mathrm{h} - R_\mathrm{Auger}(n_\mathrm{e}n_\mathrm{h}n_\mathrm{h} + n_\mathrm{e}n_\mathrm{e}n_\mathrm{h}) \tag{3}$$

$$\frac{\mathrm{d}n_\mathrm{T}}{\mathrm{d}t} = +R_\mathrm{pop}(N_\mathrm{T} - n_\mathrm{T})n_\mathrm{e} - R_\mathrm{detrap}n_\mathrm{T} - R_\mathrm{depop}n_\mathrm{T}n_\mathrm{h}. \tag{4}$$

Through explicitly treating the trapping and depopulation processes in trap-mediated recombination, we are able to describe the rapid initial PL transient decays observed in low fluence PL transient decay measurements.

In Figure S13, we show resulting fits of the model to the measured PL transients at temperatures from 50 K to 295 K. We excluded temperatures below 50 K from fitting as in this regime band-tail PL emission results in qualitatively different charge carrier dynamics.

Model parameters are discussed in Section 8. Charge-carrier accumulation and its impact on PL transients is discussed in more detail in Section 10.

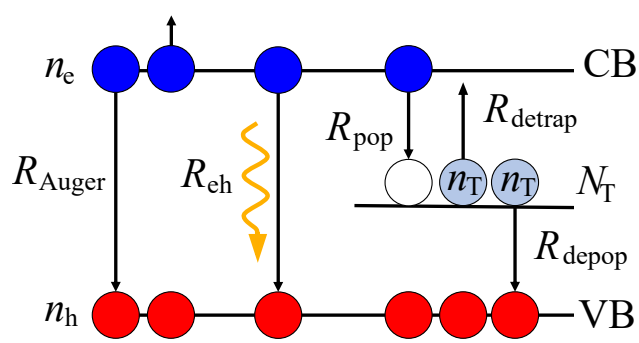

Figure S12: Schematic representation of the trap-mediated recombination model applied in this study. Free charge-carriers with density n_e in the conduction band (CB) recombine through radiative bimolecular recombination with rate constant R_{eh} or via Auger recombination, R_Auger. Furthermore, free charge-carriers in the CB populate the free trap states with rate constant R_pop. Trapped charge-carriers with density n_T recombine with holes with density n_h in the valence band (VB) with a rate constant R_depop or trapped charge-carriers de-trap with a rate constant R_detrap to return as free charge-carriers to the CB. The total trap density is given by N_T.

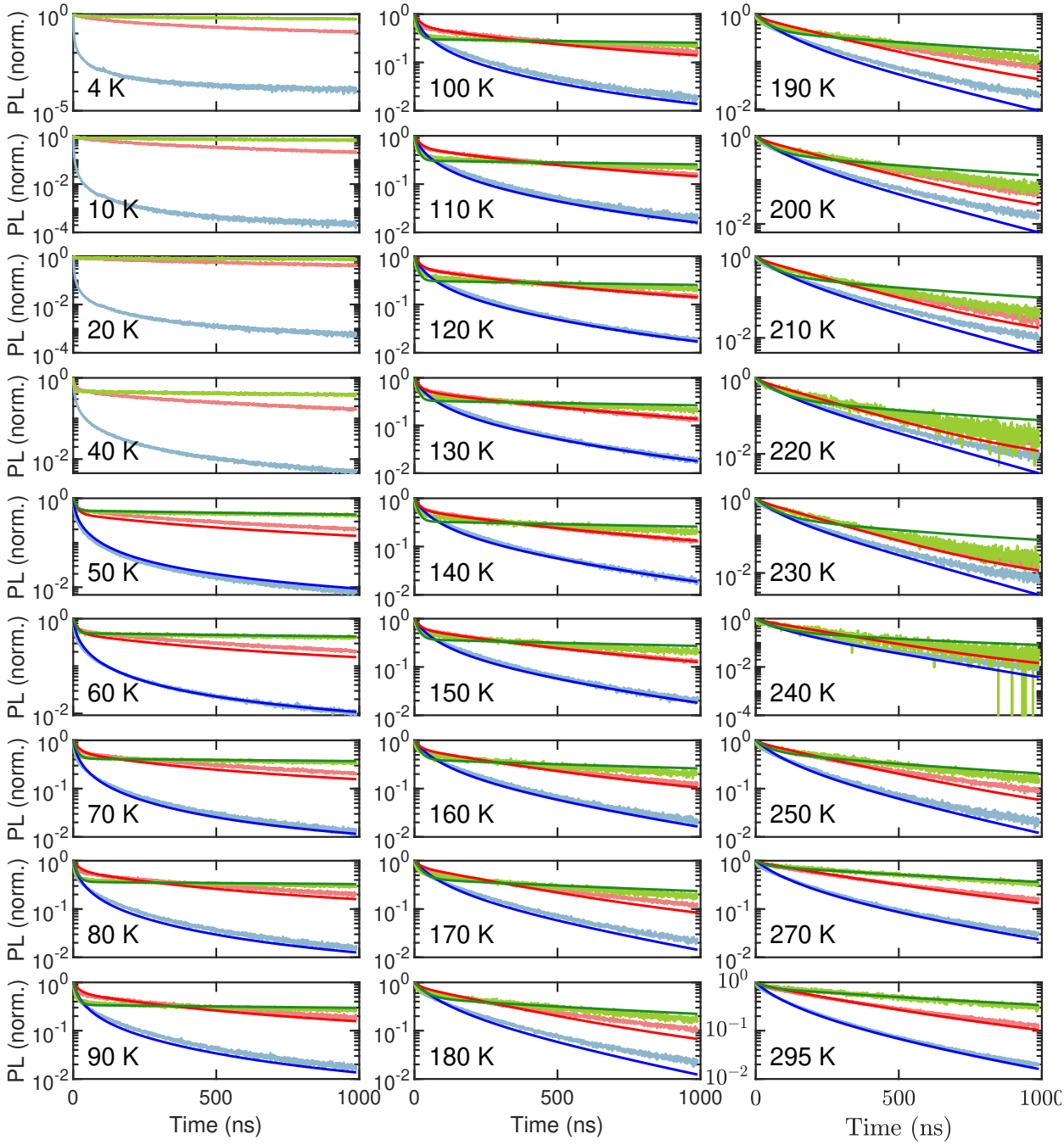

Figure S13: $FA_{0.95}Cs_{0.05}PbI_3$ thin film. Fits to PL transients following the extended trap-mediated recombination model. The sample was photoexcited at 398 nm at fluences of 3.6 nJ/cm^2 (green), 34 nJ/cm^2 (red), 280 nJ/cm^2 (blue). Experimental data at each fluence is shown in corresponding faded colors to the fits. PL was detected at its peak emission wavelength. Model parameters of the fitted curves are summarized in Table S1.

8 Model parameters

The explicit trap-mediated recombination model is a many-parameter model. We narrow down the parameter space by deriving the temperature dependence of the bimolecular recombination constant and by considering the treatment of trap-related parameters. These assumptions on the different rate constant and trap parameters are discussed in the following. Values returned by the fits are summarized in Table S1.

Table S1: Summary of parameters calculated or returned from fits to PL transient data based on the explicit charge-trapping model described in the text. The depopulation rate constant R_{depop}, Auger recombination rate constant R_{Auger} and the de-trapping rate R_{detrap} are fitted globally across different fluences at each individual temperature. Global fits to PL transients across all temperatures and fluences resulted in a trap population rate constant $R_{\mathrm{pop}} = (8.2 \pm 0.1) \times 10^{-9}\,\mathrm{cm}^3/\mathrm{s}$ independent of temperature. The trap density N_{T} is also globally fitted across fluence and temperature, where $N_{\mathrm{T}}(T)$ has four fitting parameters $N_{\mathrm{T}}(N_0, \Delta N, b, T_{\mathrm{shift}}) = N_0 + \Delta N / \left(1 + \exp\left(-b\left(T - T_{\mathrm{shift}}\right)\right)\right)$. The relative bimolecular recombination constant R_{eh} was determined based on the PL emission right after laser excitation from PL transient measurement and was scaled to room temperature measurements of R_{eh} using the absolute value determined by optical-pump THz-probe photoconductivity spectroscopy.

T (K)	R_{depop} (cm^3/s)	R_{eh} (cm^3/s)	R_{Auger} (cm^6/s)	R_{detrap} (1/s)	N_T (1/cm^3)
50	1.12×10^{-13}	1.86×10^{-10}	5.77×10^{-27}	$9.32\times10^{+06}$	$1.63\times10^{+16}$
60	1.20×10^{-13}	1.52×10^{-10}	4.49×10^{-27}	$6.14\times10^{+06}$	$1.63\times10^{+16}$
70	1.39×10^{-13}	1.26×10^{-10}	3.85×10^{-27}	$3.29\times10^{+06}$	$1.63\times10^{+16}$
80	1.30×10^{-12}	1.06×10^{-10}	3.85×10^{-27}	$2.47\times10^{+06}$	$1.63\times10^{+16}$
90	4.88×10^{-12}	9.08×10^{-11}	4.03×10^{-27}	$2.69\times10^{+06}$	$1.63\times10^{+16}$
100	9.98×10^{-12}	7.84×10^{-11}	4.23×10^{-27}	$2.81\times10^{+06}$	$1.62\times10^{+16}$
110	1.15×10^{-11}	6.83×10^{-11}	3.68×10^{-27}	$2.94\times10^{+06}$	$1.61\times10^{+16}$
120	1.44×10^{-11}	6.00×10^{-11}	3.54×10^{-27}	$3.19\times10^{+06}$	$1.58\times10^{+16}$
130	1.91×10^{-11}	5.32×10^{-11}	3.39×10^{-27}	$3.85\times10^{+06}$	$1.52\times10^{+16}$
140	2.44×10^{-11}	4.75×10^{-11}	3.13×10^{-27}	$3.80\times10^{+06}$	$1.39\times10^{+16}$
150	3.86×10^{-11}	4.27×10^{-11}	3.18×10^{-27}	$4.52\times10^{+06}$	$1.15\times10^{+16}$
160	7.61×10^{-11}	3.86×10^{-11}	2.73×10^{-27}	$4.90\times10^{+06}$	$8.50\times10^{+15}$
170	1.50×10^{-10}	3.52×10^{-11}	2.46×10^{-27}	$4.53\times10^{+06}$	$5.79\times10^{+15}$
180	2.88×10^{-10}	3.21×10^{-11}	1.91×10^{-27}	$4.92\times10^{+06}$	$4.06\times10^{+15}$
190	4.64×10^{-10}	2.95×10^{-11}	1.97×10^{-27}	$3.79\times10^{+06}$	$3.18\times10^{+15}$
200	6.55×10^{-10}	2.73×10^{-11}	1.83×10^{-27}	$3.22\times10^{+06}$	$2.79\times10^{+15}$
210	8.02×10^{-10}	2.52×10^{-11}	2.08×10^{-27}	$2.60\times10^{+06}$	$2.62\cdot10^{+15}$
220	9.35×10^{-10}	2.35×10^{-11}	1.93×10^{-27}	$2.25\times10^{+06}$	$2.55\times10^{+15}$
230	9.68×10^{-10}	2.19×10^{-11}	2.65×10^{-27}	$2.30\times10^{+06}$	$2.52\times10^{+15}$
240	8.65×10^{-10}	2.05×10^{-11}	2.61×10^{-27}	$2.14\times10^{+06}$	$2.51\times10^{+15}$
250	5.98×10^{-10}	1.93×10^{-11}	2.04×10^{-27}	$4.90\times10^{+06}$	$2.50\times10^{+15}$
270	4.55×10^{-10}	1.71×10^{-11}	1.67×10^{-27}	$1.04\times10^{+07}$	$2.50\times10^{+15}$
295	5.83×10^{-10}	1.50×10^{-11}	2.13×10^{-27}	$1.20\times10^{+07}$	$2.50\times10^{+15}$

8.1 Initial charge-carrier density

The charge-carrier decays and resulting PL transients that are calculated using rate equations 3 and 4 depend on the kinetics of free and trapped charge-carrier densities. The total decay rates at any point in time are calculated based on the current number of charge-carriers in the model system. Therefore, we carefully determine the initial charge-carrier density at the time of laser excitation, in order to predict the decay rates as a function of time.

The charge-carrier density n_0 that is added to the model system at each excitation pulse arrival, is calculated based on the number of photons absorbed by the perovskite thin film, following:

$$n_0 = a_{\text{absorbed}} \frac{\lambda_{\text{laser}}}{hc} \frac{P_{\text{laser}}}{f_{rep}} \frac{1}{dA_{\text{ill}}} \tag{5}$$

with the power of the laser P_{laser}, the fraction of absorbed photons $a_{\text{absorbed}} \approx 1$, the area of illumination $A_{\text{ill}} = 4.5 \times 10^{-2}\,\text{mm}^2$, excitation wavelength $\lambda_{\text{laser}} = 398\,\text{nm}$, the repetition rate of the laser $f_{\text{rep}} = 1\,\text{MHz}$ and the thickness of the sample $d = (585 \pm 8)\,\text{nm}$ for $FA_{0.95}Cs_{0.05}PbI_3$ and $d = (540 \pm 5)\,\text{nm}$ for $FA_{0.83}Cs_{0.17}PbI_3$. The sample thickness is determined by scratching the samples with a razor blade down to the z-cut quartz crystal substrate and measuring the resulting scratch profile using a Veeco Dektak 150 profilometer. Both samples showed little thickness variation across the thin film. The calculations of n_0 assume a spatially homogeneous charge-carrier density through the film profile. It has previously been shown that the charge-carriers homogeneously distribute via diffusion and photon recycling processes within a few nanoseconds, justifying this assumption.[S28] The area of illumination is given by the spot size of the excitation laser with a Gaussian beam profile. The standard deviation is set as the limit of the beam size. The resulting charge-carrier densities at different excitation fluences are summarized in Table S2.

Table S2: Summary of laser power P_{laser}, excitation fluence and corresponding charge-carrier density at a pulse repetition rate of 1 MHz for $FA_{0.95}Cs_{0.05}PbI_3$ and $FA_{0.83}Cs_{0.17}PbI_3$.

Sample	**Power** (μW)	n_0 (cm^{-3})	**Fluence** (nJ/cm^2)
$FA_{0.95}Cs_{0.05}PbI_3$	1.6	4.0×10^{14}	3.6
	15	3.9×10^{15}	34
	124	3.1×10^{16}	280
$FA_{0.83}Cs_{0.17}PbI_3$	1.5	3.9×10^{14}	3.3
	13	3.8×10^{15}	30
	111	3.0×10^{16}	260

8.2 Bimolecular recombination rate constant R_{eh}

The bimolecular recombination rate constant is measured at room temperature using optical-pump-terahertz-probe spectroscopy. The relative temperature dependence of the bimolecular recombination rate constant is derived by relating instantaneous PL upon photoexcitation with the bimolecular rate constant. The bimolecular recombination rate along temperature is then scaled using the room temperature measurement.

Determination of the bimolecular recombination rate constant at room temperature using Optical-pump-terahertz-probe spectroscopy. An amplified laser system (Spectra Physics, MaiTai Ascend Spitfire), with a 5 kHz repetition rate, centre wavelength of 800 nm and pulse duration of 35 fs was used to generate THz radiation via the inverse-spin Hall effect from an emitter made of 2 nm of tungsten / 1.8 nm of Co40Fe40B20 / 2 nm of platinum, supported by a quartz substrate. The THz probe was focused onto the sample and detected via free-space electro-optical sampling in a ZnTe(110) crystal of thickness 200 µm. A 400 nm pump pulse was generated using a Beta Barium Borate (BBO) crystal. Transient photoconductivity decays were measured by recording the change in peak THz amplitude transmitted as a function of pump-probe delay time. Measurements were carried out under vacuum ($< 1 \times 10^{-2}$ mbar).

Here, the overall charge-carrier dynamics in a perovskite semiconductor can be approximately described by the following differential equation:

$$\frac{\mathrm{d}n}{\mathrm{d}t} = -R_{\mathrm{SRH}}n - R_{\mathrm{eh}}n^2 - R_{\mathrm{Auger}}n^3. \tag{6}$$

In contrast to the PL decays discussed in the main paper, higher fluences are applied, and thus, trap-mediated recombination is not the dominant recombination channel over the nanosecond observation window of these measurements. Furthermore, as the number of

trap states is unchanged only a small fraction of free charge carriers is trapped upon excitation due to the higher excitation fluence. Therefore, no rapid initial decay is observed that needs special treatment via an explicit trapping model. While trap-mediated recombination is not dominant, we obtain values for the trap-mediated recombination constant R_{SRH} by approximating Equation 6 and fitting it to low fluence PL transient measurements in Section 6. At low excitation fluences higher-order recombination can be neglected and Equation 6 reduces to

$$\frac{\mathrm{d}n}{\mathrm{d}t} = -R_{\mathrm{SRH}} n \tag{7}$$

In this approximation a simple exponential describes the charge-carrier decay

$$n(t) = n_0 \exp(-R_{\mathrm{SRH}} t) \tag{8}$$

with n_0 the initial charge-carrier density. Despite monomolecular recombination dominating the recombination process in the low fluence regime, the PL originates from bimolecular recombination. Hence, the PL intensity $I(t)$ is governed by

$$I(t) \propto R_{\mathrm{eh}} \cdot n(t)^2 \tag{9}$$

$$\propto R_{\mathrm{eh}} \cdot n_0^2 \cdot \exp(-2R_{\mathrm{SRH}} t) \tag{10}$$

At 295 K this results in $R_{\mathrm{SRH}} = 1.2 \times 10^6\,\mathrm{s}^{-1}$ when Equation 10 is fit to PL transients at $3.6\,\mathrm{nJ/cm^2}$.

To obtain an estimated value for R_{eh} at room temperature, we use Equation 6, and set $R_{\mathrm{Auger}} = 0$ and $R_{\mathrm{SRH}} = 1.2 \times 10^6\,\mathrm{s}^{-1}$. The resulting PDE can be solved analytically:

$$\frac{\mathrm{d}n}{\mathrm{d}t} = -R_{\mathrm{SRH}} n - R_{\mathrm{eh}} n^2 \tag{11}$$

This has a solution given by

$$n(t) = \frac{R_{\mathrm{SRH}} B}{e^{R_{\mathrm{SRH}} t} - R_{\mathrm{eh}} B} \tag{12}$$

We can relate B to the initial charge-carrier density n_0 via:

$$\frac{1}{B} = \frac{R_{\mathrm{SRH}}}{n_0} + R_{\mathrm{eh}} \tag{13}$$

Thus, at $t = 0$, we recover $n(t = 0) = n_0$.

The change in transmitted THz radiation $\Delta T/T(t) = x(t)$ is proportional to the free charge-carrier density in the thin film:

$$n(t) = \Phi C x(t) \tag{14}$$

Here Φ indicates the number of free charge-carriers generated per photon, and $C = n_{0,abs}/x(0)$ is the proportionality factor between the initial THz response x(0) and the absorbed photon density $n_{0,abs}$, given by:

$$n_{0,abs} = \frac{E\lambda}{hcA_{\mathrm{eff}}} \left(1 - R_{\mathrm{pump}}(\lambda)\right) \left(1 - T_{\mathrm{pump}}(\lambda)\right) \tag{15}$$

with the laser pump wavelength $\lambda = 400\,\mathrm{nm}$ and E the laser power. Here the effective overlap area $A_{\mathrm{eff}} = 0.28\,\mathrm{cm}^2$ can be calculated from the pump and probe beam parameters, whilst the transmission $T_{\mathrm{pump}} = 0.003$ and reflection coefficients $R_{\mathrm{pump}} = 0.01$ are measured for each sample, using a Fourier transform infrared spectrometer (Bruker Vertex 80v). For very high excitation fluences ($> 50\,\mu\mathrm{J/cm}^2$) the proportionality in Equation 14 no longer holds; we therefore determine C based on the initial response for fluences below this. Substituting

Equation 14 into 11 gives us:

$$\frac{\mathrm{d}x}{\mathrm{d}t} = -C\Phi R_{\mathrm{eh}} x^2 - R_{\mathrm{SRH}} x \tag{16}$$

$$= -A_2 x^2 - A_1 x \tag{17}$$

Analytical solutions to this ODE are fitted globally to the decays across all fluences in order to extract the rate constants A_i. Given the influence of the photon-to-free-charge conversion ratio Φ we can only determine apparent bimolecular recombination rates ΦR_{eh}. Given the low exciton binding energy in these materials,[S29-S33] we may however assume that $\Phi \sim 1$. Finally, in order to account for an initial spatially varying charge-carrier density (due to absorption following the Beer-Lambert law), the fitting algorithm takes into account an exponentially decaying charge-carrier density. This is done by dividing the sample into 30 equally thick slices and computing the decay function for each of these individually.

The fit resulted in $R_{\mathrm{eh}} = (1.5 \pm 0.2) \times 10^{-11}\,\mathrm{cm}^3/\mathrm{s}$, base on the assumption of a trap-mediated recombination constant $R_{\mathrm{SRH}} = 1.2 \times 10^6\,\mathrm{s}^{-1}$, as obtained from fits of PL transient measurements.

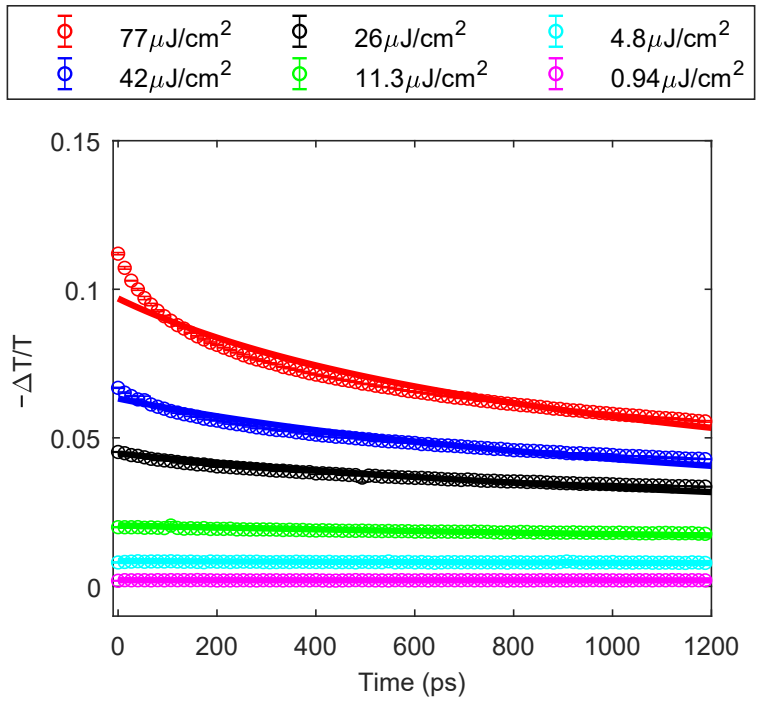

Figure S14: Fits of Equation 17 (solid lines) to THz decay traces (open symbols) for a thin film of $FA_{0.95}Cs_{0.05}PbI_3$, measured at room temperature. From these fits a bimolecular recombination rate of $R_{\mathrm{eh}} = (1.5 \pm 0.2) \times 10^{-11}\,\mathrm{cm}^3/\mathrm{s}$ is obtained, under the assumption of $R_{\mathrm{SRH}} = 1.2 \times 10^6\,\mathrm{s}^{-1}$.

Temperature dependence of the bimolecular recombination rate constant. The instantaneous PL emission has been linked to the bimolecular recombination constant R_{eh} by Sarritzu *et al.*[S34] Assuming that only bimolecular recombination is radiative, the PL intensity $I(t)$ is proportional to the total rate of bimolecular recombination

$$I(t) \propto R_{eh} n_e(t) n_h(t) \tag{18}$$

at all times. At $t = 0$ the initial charge-carrier density is given by the photoexcitation, i.e. $n(t = 0) = n_0$, given that no recombination has as yet occurred. In the high fluence regime we assume $n_0 = n_e = n_h$, and hence $I_0 \propto R_{\mathrm{eh}} \cdot n_0^2$. The injected charge-carrier density n_0 upon excitation is identical at all temperatures and hence we obtain a temperature dependent relationship between the bimolecular recombination constant and the instantaneous PL intensity immediately after photoexcitation I_0

$$I_0(T) \propto R_{\mathrm{eh}}(T) \cdot n_0^2 \tag{19}$$

$$\Rightarrow I_0(T) \propto R_{\mathrm{eh}}(T). \tag{20}$$

We determine the instantaneous PL response $I_0(T)$ by determining the early-time value $I_{0,\mathrm{TCSPC}}$ immediately flowing excitation, at the detection energy of PL transients and correcting for changes in spectral emission broadening with temperature.

The instantaneous PL emission of PL transients $I_{0,\mathrm{TCSPC}}$ is calculated by integrating over the initial decay of the PL transients within 3 ns before significant charge-carrier recombination has occurred. The detection energy for PL transients was set to the PL maximum determined by time-integrated PL spectra.

The PL spectra broaden with increasing temperature, while the PL transients only record the PL decay at the detection wavelength. Therefore, the initial PL intensity was corrected for the spectral broadening with temperature. For this purpose, the PL spectra $I(\lambda)$ were

approximated by a Gaussian:

$$I(\lambda) = I_{\max} \exp\left(-\frac{(\lambda - \lambda_{\max})}{2\sigma_{\mathrm{PL}}}\right)^2 \tag{21}$$

with the PL intensity $I_{\max}$ at the peak emission wavelength $\lambda_{\max}$ and the standard deviation σ_{PL}. The total emission of photons scales with its peak intensity $I(\lambda_{\max})$ and standard deviation σ_{PL} following

$$\int I(\lambda)\mathrm{d}\lambda \propto I(\lambda_{\max}) \cdot \sigma_{\mathrm{PL}}. \tag{22}$$

The total radiative PL emission is proportional to the radiative term of the rate equation $\int I(\lambda)\mathrm{d}\lambda \propto R_{\mathrm{eh}} n_e n_h$ and the peak PL intensity is proportional to the instantaneous PL from PL transients $I(\lambda_{\max}) \propto I_{0,\mathrm{TCSPC}}$.

Hence, the bimolecular recombination rate constant R_{eh} can be expressed by

$$R_{\mathrm{eh}}(T) \propto I_{0,\mathrm{TCSPC}}(T) \cdot \sigma_{\mathrm{PL}} \tag{23}$$

We confirmed that the PL transients at different detection energies along the PL spectra show the same decay dynamics and therefore a comparison between spectral width of time-integrated PL spectra and PL width at instantaneous PL emission is valid.

We choose high fluence PL transients to determine the instantaneous PL. For modelling the charge-carrier decays, we take into account charge-carrier accumulation after multiple excitation cycles. At high excitation fluence and corresponding charge-carrier densities, the charge-carrier decay is fast and a large fraction of the carriers initially present will decay prior to the arrival of the following excitation pulse; therefore we assume that $n_0(t = 0) \approx n_e(t = 0)$. Furthermore, bimolecular recombination is sensitive to the electron n_e and hole density $n_h = n_e + n_T$. At low excitation fluence the free hole density is considerably larger than the free electron density, due to a large number of filled trap states. At high charge-

carrier densities, the difference between holes and electron becomes negligible $n_h \approx n_e$. Such conditions are met by high excitation fluences right after photoexcitation. Ultimately, low fluence PL transients exhibit a fast decay component that rapidly reduces the PL intensity within nanoseconds and therefore low fluence measurements are not suitable for determining instantaneous PL here.

Relating the instantaneous PL to the bimolecular recombination rate gives us a relative value of the bimolecular recombination rate constant across temperatures.

We fit the relative bimolecular recombination constant to a previously used phenomenological function that describes the bimolecular recombination constant of $MAPbI_3$[S35]

$$R_{\mathrm{eh}}(T) = C\ e^{\frac{a}{b+T}}; \tag{24}$$

and obtain $a = 1169\,\mathrm{K}$ and $b = 186\,\mathrm{K}$. Using THz measurements we can set the bimolecular rate constant to $R_{\mathrm{eh}} = (1.5 \pm 0.2) \times 10^{-11}\,\mathrm{cm}^3/\mathrm{s}$ at room temperature, as described previously in this section. The bimolecular recombination rate constant R_{eh} determined in this way across temperature is shown in Figure S15.

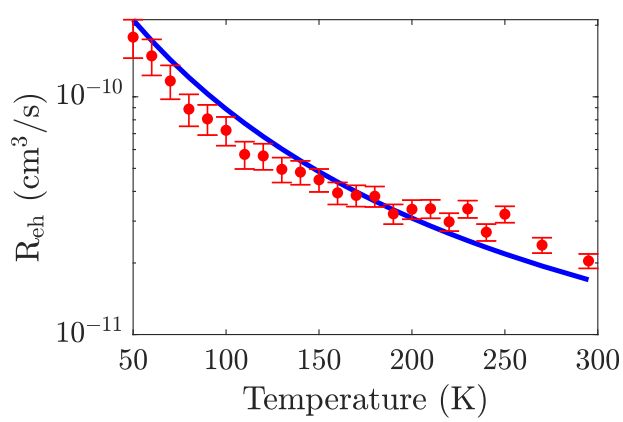

Figure S15: Bimolecular recombination rate constant for a $FA_{0.95}Cs_{0.05}PbI_3$ thin film obtained across different temperatures from instantaneous PL intensity values obtained from PL transients, and scaled by the value at room temperature obtained from THz photoconductivity measurements. Fits of Equation 24 (solid blue line) to measured instantaneous PL (red circles).

9 Model outputs

9.1 PL transient decays

Figure S16 shows the model PL transients that follow from fitting the explicit trap-mediated recombination model to the experimental PL transients at high and low fluence. In Figure S11, we presented the same graph, but for the experimental PL transients. The model is able to describe the experimental data well. We point out that the model is able to reproduce initial decays at low fluence that show faster and larger PL transient decays at low temperatures as compared to high temperatures, as shown in Figure S16. This is not the case if a constant trap density is assumed, as discussed further in Section 11.

Furthermore, we compare the absolute PL transient decay intensity from our model with the measured PL transient intensity; see Figure S17. The relative intensity across temperature is also well described by the model, suggesting that the radiative recombination channels have been addressed correctly, while the PL transients at each temperature agree well in their temporal decay.

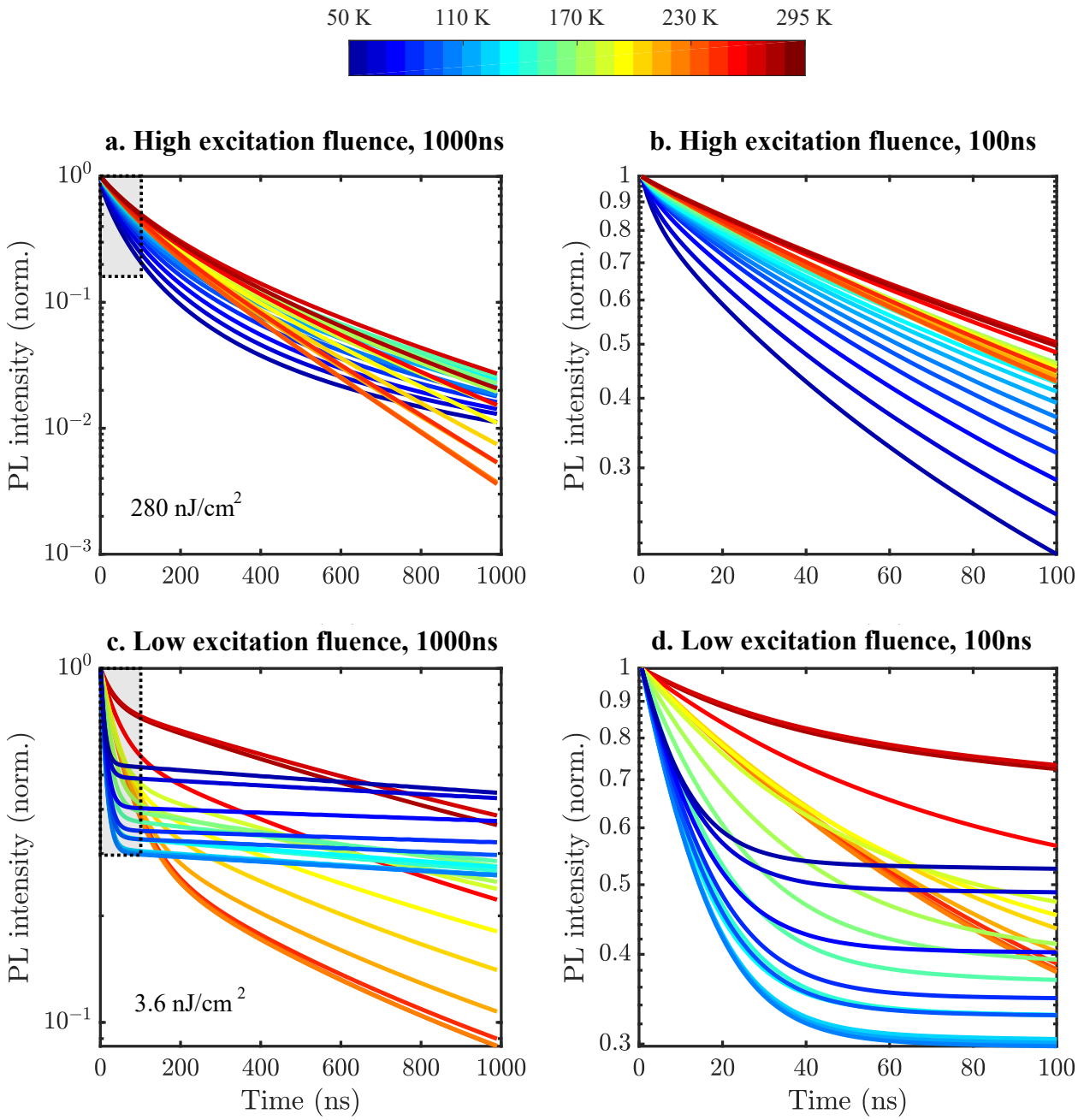

Figure S16: Normalized PL transient measurements returned by the model, for fits to data for high (a, b) and low (c, d) fluence excitation from 50 K to 295 K for a $FA_{0.95}Cs_{0.05}PbI_3$ thin film. The overall decay within each excitation cycle is shown on the left at a excitation pulse frequency of 1 MHz. The small box indicates the time scale of the figures on the right, up to 100 ns. Figure (d) shows a fast decay component in low excitation fluence PL transient measurements. The rapid initial decay becomes more dominant at lower temperatures.

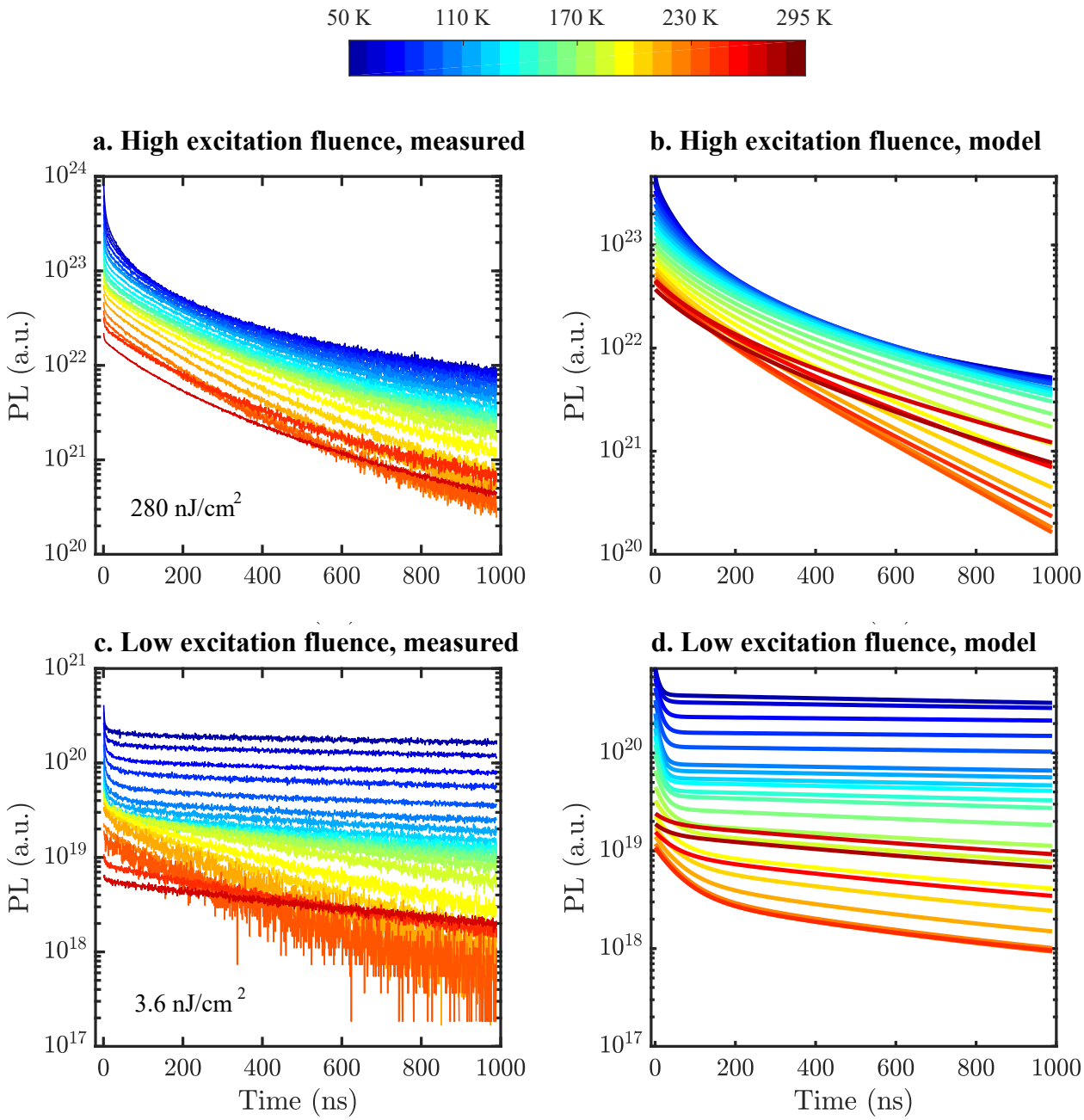

Figure S17: Non-normalized PL transients experimentally determined (left) and modelled (right) at the corresponding excitation fluence at temperatures ranging from 50 K to 295 K of a $FA_{0.95}Cs_{0.05}PbI_3$ thin film. All modelled data is shifted by a scaling factor to match the experimental output. Our model has previously shown that is able to reproduce the kinetics of PL transient decays. Here we show that additionally the absolute PL intensity is also well represented.

9.2 Recombination rates

In Figure S18 we compare the individual contributions to the overall charge-carrier population decay rates for each recombination mechanism. The bimolecular recombination rate $R_{\mathrm{eh}} n_e n_h$ is proportional to the PL intensity that we observe in PL transient measurements. We find that charge-carrier trapping and de-trapping are fast processes. Immediately following photoexcitation, a large number of free carriers is initially generated. At the same time, trap states have become unoccupied due to depopulation prior to the arrival of the new laser excitation pulse. Therefore, free carriers are readily trapped in unoccupied traps and the initial population of trap states occurs very fast. Such trapping continues until trap filling is balanced by de-trapping. Once trap-population, governed by R_{pop}, and de-trapping, governed by R_{detrap}, reach a quasi-equilibrium, the trap population rate and de-trapping rate balance each other and only a relatively low net trapping rate ΔR_{trap} remains, $\Delta R_{trap} = R_{\mathrm{pop}}(N_{\mathrm{T}} - n_{\mathrm{T}})n_{\mathrm{e}} - R_{\mathrm{detrap}} n_{\mathrm{T}}$ remains. The net trapping rate also depends on how fast traps depopulate via recombination with holes in the valence band.

Only at high temperature and high fluence (Figure S18b) is the depopulation rate $R_{\mathrm{depop}} n_T n_h$ sufficiently high to exhibit a significant difference between $R_{\mathrm{pop}}(N_T - n_T)n_e$ and $R_{\mathrm{detrap}} n_T$, meaning that no such quasi-equilibrium between trapping and de-trapping is reached. In this scenario traps, are nearly completely filled, hence the detrapping rate cannot further increase. The trap population is hence initially large, but slowly decreases over time as the number of free carriers in the CB n_e decreases.

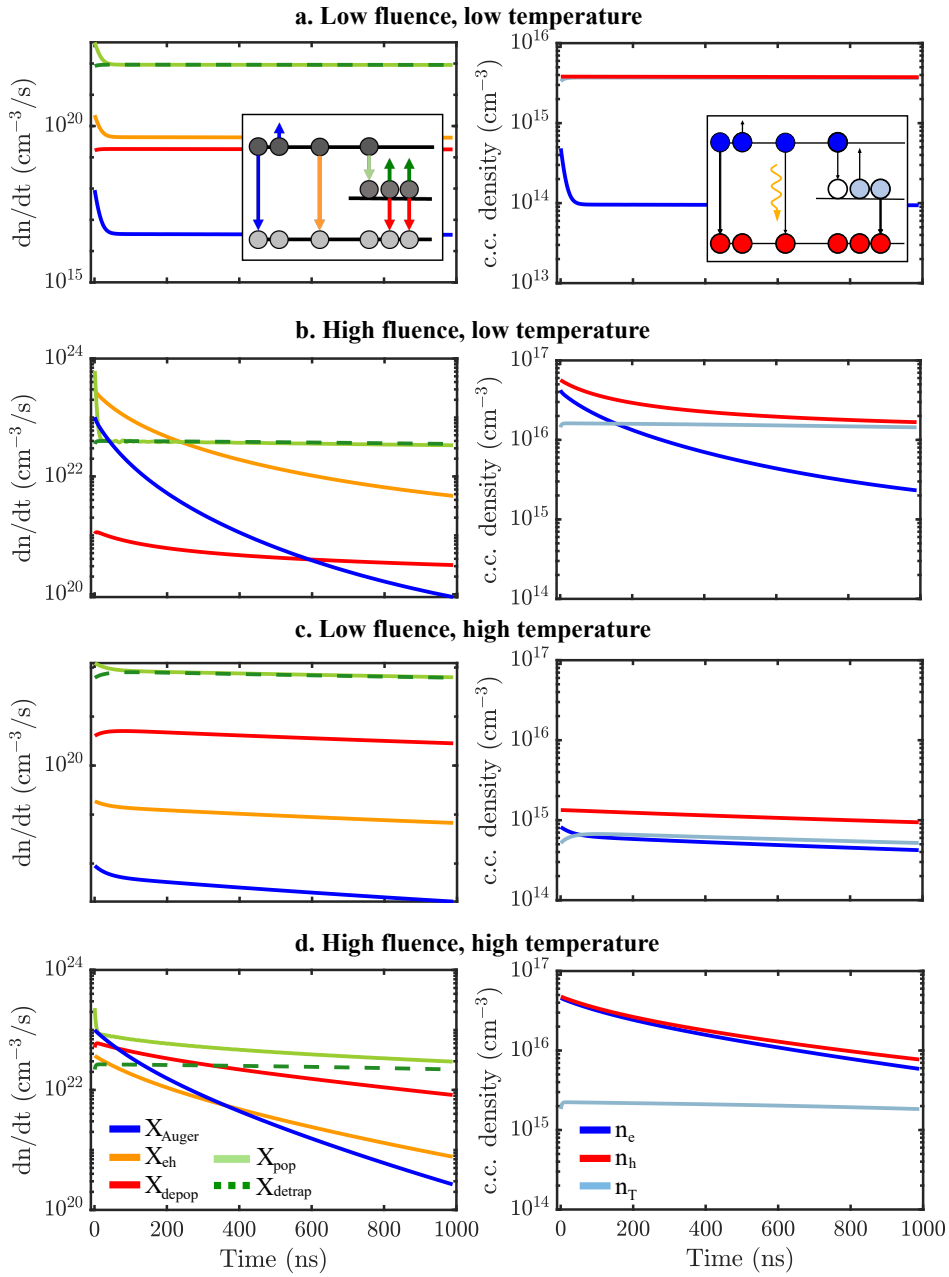

Figure S18: $FA_{0.95}Cs_{0.05}PbI_3$ thin film. Left: Individual recombination rates at high (280 nJ/cm^2, b. & d.) and low (3.6 nJ/cm^2, a. & c.) excitation fluence, and high (295 K, c. & d.) and low (80 K, a. & b.) temperature. Auger recombination $X_{\mathrm{Auger}} = R_{\mathrm{Auger}}(n_e n_e n_h + n_e n_h n_h)$, bimolecular recombination $X_{\mathrm{eh}} = R_{\mathrm{eh}} n_e n_h$, trapped-carrier to hole recombination $X_{\mathrm{depop}} = R_{\mathrm{depop}} n_{\mathrm{T}} n_h$, detrapping $X_{\mathrm{detrap}} = R_{\mathrm{detrap}} n_T$ and trap population rate $X_{\mathrm{pop}} = R_{\mathrm{pop}} n_e (N_T - n_T)$. The PL transients are proportional to the bimolecular recombination rate X_{eh}. Right: Corresponding charge-carrier densities. Free electron density in the CB, n_e, trapped electron density in sub-band gap states, n_T, and free hole density in the VB, n_h.

10 Charge-carrier accumulation and trap saturation

The charge-carrier dynamics in the proposed model depend on the kinetics of free and trapped charge-carrier densities. In Section 7 we model the charge-carrier dynamics using a rate equation. In this approach, charge-carrier densities evolving over time depend on the initial charge-carrier densities in the model system. Therefore, an assessment of the initial charge-carrier densities is essential. The initial free and trapped charge-carrier densities are determined by the free charge-carriers that are added to the system by repeated laser pulses and by the charge-carriers that remain in the system through incomplete decay between consecutive laser pulses.

In time-correlated single photon counting (TCSPC) we accumulate measurements over many repeated excitation cycles, and hence we observe the decay of charge-carriers for a semiconductor that has been illuminated over numerous excitation cycles. As the charge-carrier dynamics and corresponding PL emission are sensitive to the charge-carrier densities, we discuss the interaction of trapped or free background charge-carriers with charge-carriers generated by the next pulse.

Previously, it has been suggested that PL intensities of charge-carriers that originated from a particular excitation cycle decay individually[S36] without interfering with those from different excitation cycles. This assumes that charge-carriers generated in different excitation cycles belong to separate charge-carrier populations and decay independently. However, there is no reason why charge-carrier densities would form such separate populations over time in these perovskite samples.

We assume that free charge-carriers and filled traps may partially remain in the system before re-excitation occurs. Free charge-carriers generated in a consecutive excitation are added to such remnant charge-carriers. Trapped charge-carriers that remain prior to excitation are also still present in the next excitation cycle regardless of renewed photoexcitation. The density of trapped charge-carriers will be further enhanced by the newly arrived charge-carriers and trapped charge-carriers will decay or de-trap until a new excitation pulse occurs.

10.1 PL transients at varying laser pulse rate

We assess the potential presence of such remnant charge carriers by measuring PL transients at different laser pulse repetition rates. This allows us to observe the influence of the densities of the charge-carriers prior to excitation on the subsequent PL decay. Depending on the laser repetition rate, charge-carriers will have decayed to various degrees and hence reach a different final density before a new excitation pulse arrives. If the next pulse follows after longer time periods, more trapped carriers will have depopulated beforehand, which results in a higher number of vacant trap sites before the new excitation pulse occurs.

We measured PL transients at 1 MHz, 250 kHz and 61.25 kHz repetition rates, as shown in Figure S19. At different laser pulse rates, various initial decays are observed, with a more pronounced initial rapid decay for lower laser repetition rate. If the prior state did not influence the charge-carrier dynamics, then all PL transients should follow the same decay after excitation, which is clearly not the case.

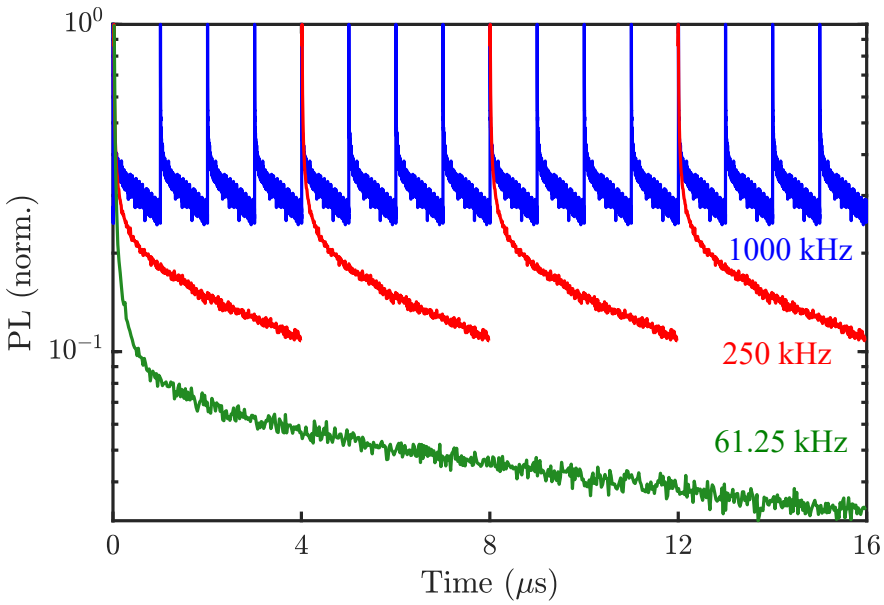

Figure S19: $FA_{0.95}Cs_{0.05}PbI_3$ thin film. PL transients recorded for laser repetition rates of 1000 kHz, 250 kHz and 61.25 kHz at 100 K at a low excitation fluence of 3.6 nJ/cm^2. At lower laser pulse repetition rates, trapped carriers have more time to depopulate, resulting in a larger number of vacant trap sites being available prior to the arrival of a consecutive laser pulse, compared to high repetition rate measurements. This results in a higher trap-related capture rate of free charge carriers.

10.2 Modelling free and trapped charge-carrier accumulation

PL transients measured at various repetition rates (Figure S19) show that the initial state of the system changes if charge-carriers are given more time to be trapped or recombine. Furthermore, this change in initial carrier density impacts the subsequent PL transient decays. In the proposed trapping model, charge-carriers which have not decayed prior to the arrival of a subsequent laser pulse remain in the model system.

In order to account for variable initial charge-carrier densities following charge-carrier accumulation, we solve the set of differential equations given by Equation 3 and 4 for multiple excitation cycles. The method is described in the following.

For solving the rate equations the **ode45** solver (MATLAB R2018a) was used. We obtain $n_{\mathrm{e}}(t)$ and $n_{\mathrm{T}}(t)$ from the rate equations by providing the initial conditions $n_{\mathrm{e}}(t = 0s) = n_{\mathrm{e,start}}$ and $n_T(t = 0s) = n_{\mathrm{T,start}}$, as well as the integration time window $T = [0\,\mathrm{ns},\ 1/f_{\mathrm{rep}}]$

with the laser repetition rate f_{rep}. Regarding notation, we enumerate excitation cycles x following $x = 1,\ 2,\ 3,$ etc. We distinguish between the carrier densities n_{start} just after photoexcitation at the beginning of the excitation cycle, and the carrier density n_{end} just before arrival of a subsequent laser pulse at the end of the excitation cycle during which some charge-carrier recombination has occurred. For the first excitation cycle $x = 1$, we assume fully unoccupied traps, or $n_{\mathrm{T},x=1,\mathrm{start}} = 0\,\mathrm{cm}^{-3}$, and a free charge-carrier density of $n_{\mathrm{e},x=1,\mathrm{start}} = n_0$, which is the charge-carrier density added with each photoexcitation. For the next pulse, we assume that trapped carriers remain in the model system, and hence, $n_{\mathrm{T},x=2,\mathrm{start}} = n_{\mathrm{T},x=1,\mathrm{end}}$. We equally assume that any remnant free carriers also remain in the model system. With each new laser pulse, the charge-carrier density n_0 is added to the free-carrier density $n_{\mathrm{e},x=2,\mathrm{start}} = n_0 + n_{\mathrm{e},x=1,\mathrm{end}}$. The end-state density for each carrier density at the edn of each cycle is calculating following the set of rate equations defining the trap-mediated recombination model outlined above (Equations 3 and 4). For a generic iteration step, we update the starting values for solving the ODEs in each iteration, following

$$n_{\mathrm{T},x=n+1,\mathrm{start}} = n_{\mathrm{T},x=n,\mathrm{end}} \tag{25}$$

$$n_{\mathrm{e},x=n+1,\mathrm{start}} = n_0 + n_{\mathrm{e},x=n,\mathrm{end}}. \tag{26}$$

All iterations are calculated using the same parameters, with the variability as described earlier for the various temperatures and excitation fluences. The iterative calculation of charge-carrier densities is carried out until $n_{\mathrm{T,start}} = n_{\mathrm{T,end}}$ and $n_{\mathrm{e,start}} = n_0 + n_{\mathrm{e,end}}$, allowing for an error between n_{start} and n_{end} of 1%. The final iteration step is used for fitting the model to the experimentally observed PL transients.

In Figure S20 the impact of charge-carrier accumulation on PL transients is shown in terms of increasing numbers of iterations in the model system as described above. We note that with increasing iterations, the PL transients converge to a stable solution. Starting with unoccupied trap states ($x = 1$), repeated laser excitation affects the charge-carrier

dynamics due to charge-carrier accumulation until an equilibrium state is reached. The PL transients initially change significantly with each additional arriving laser pulses, but eventually converge with an increasing number of iterations. While at high fluence, the effect of charge accumulation on the PL transient is low, it significantly changes the dynamics of low-fluence measurements because the impact of the initial trap density is larger. At low fluence, if all traps are empty and the trap density is of the same order as the charge-carrier density added per excitation pulse, $n_{\mathrm{e}} \approx N_{\mathrm{T}}$, then almost all free charge-carriers become trapped very fast and the PL decays quickly due to $I(t) \propto n_{\mathrm{e}}(t) n_{\mathrm{h}}(t)$.

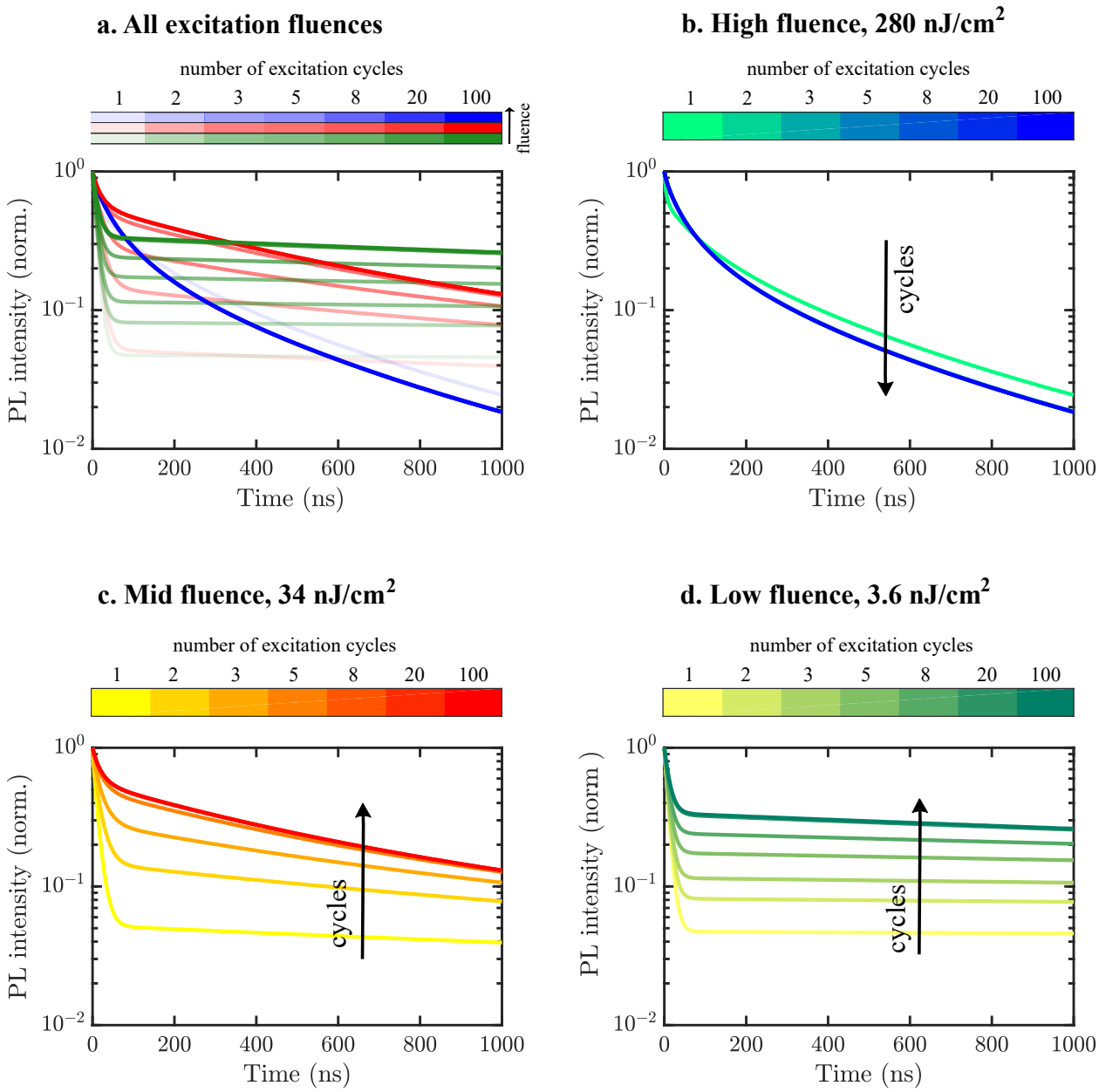

Figure S20: $FA_{0.95}Cs_{0.05}PbI_3$ thin film. Modelling charge-carrier accumulation within repeating excitation cycles. (a) Three fluences are shown: low (3.6 nJ/cm^2, green), mid (34 nJ/cm^2, red), high (280 nJ/cm^2, blue). Lightly faded colors correspond to few repetition cycles, darker tones correspond many repetition cycles. The more laser cycles have passed, the more traps states are filled. In (b), (c) and (d) the decays for each fluence are shown. The arrow indicates an increasing number of excitation cycles simulated by the model. For the high-fluences case (b) all but the curve calculated for the first cycle lie on top of each other.

Additionally, we apply the our trapping model to the measurements at varying repetition rates shown in Figure S19. The model was applied to PL transients at 1 MHz through global

fits across different temperatures and three excitation fluences, as discussed in the main article. The parameters resulting from fits, summarized in Table S1, can be applied to model the dynamics at different repetition rates according to the accumulation method described above. Therefore, the independent variable is the time allowed for charge-carriers to decay prior to a repeated photoexcitation. In our model this corresponds to the integration time window $T = [0\,\mathrm{ns},\ 1/f_{\mathrm{rep}}]$. All other parameters are the same as reported in previous sections. Calculated PL transients for different repetition rates agree well with measured transients, as seen in Figure S21. The charge-carrier trapping model is thus well able to describe charge-carrier accumulation effects in trap states. The free charge-carrier density decreases over time along with the trapped charge-carrier density. If the consecutive pulse follows after longer time periods, more trapped carriers depopulate and a higher number of vacant trap sites is available before the new excitation pulse occurs. A higher number of vacant trap states results in a larger number of initially trapped charge-carriers, and ultimately, results in a larger decay in the initial PL transients. The PL intensity is determined by the charge-carrier density as $I(t) \propto R_{\mathrm{eh}} n_{\mathrm{e}}(t) n_{\mathrm{h}}(t)$ and as such, is very sensitive to changes in the carrier density. The rapid PL decay is explained by rapidly decreasing charge-carrier densities caused by the quick trapping of free charge-carriers.

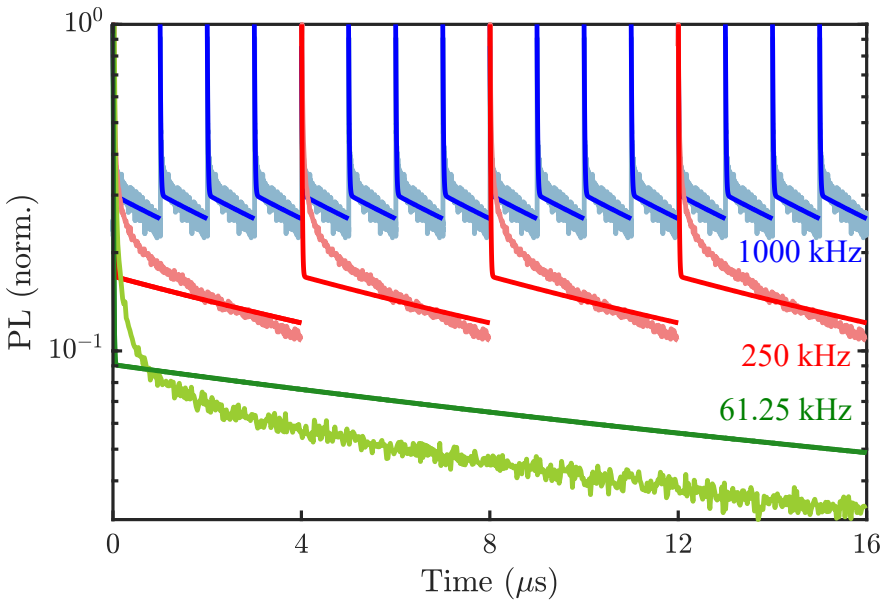

Figure S21: $FA_{0.95}Cs_{0.05}PbI_3$ thin film. Measured (faded colors) and calculated (bright colors) PL transient decays for laser repetition rates of 1000 kHz, 250 kHz and 61.25 kHz at 100 K at a low excitation fluence of 3.6 nJ/cm^2. Model parameters were obtained from fits of model solutions to PL transients at 1000 kHz across temperature. The same parameters were then used for calculating PL transient decays at different repetition rates. At lower pulse repetition rate, more trap states are unoccupied prior to each subsequent laser pulse, and hence, a larger number of charge-carriers can initially be trapped, resulting in larger initial PL decays. We note that the calculated PL transients at 250 kHz and 61.25 kHz show a sharp decay that is not reflected in the experimental data. We attribute this to the assumption of a single trap state with a single de-trapping and depopulation rate. At longer time scales, trap states with varying parameters may be occupied that are not reflected in the model. Calculated PL decays for 250 kHz and 61.25 kHz are not result of fits, but are calculated from the parameters obtained at 1000 kHz. However, these show a qualitative agreement of model and experiment that relates to charge-carrier accumulation.

11 Constant trap density - a comparison

In the main text we propose that a change in trap density centred at the phase transition can account for the temperature dependence of the rapid charge-carrier decay following pulsed photoexcitation. In the following we perform an analysis of a model system that assumes a constant trap density across all temperatures and we compare it to our proposed model that assumes a varying trap density.

We make the same parameter assumptions as discussed in Section 8, excluding the assumptions about the trap density N_T. Previously we assumed two distinct trap densities at high and low temperature. For the constant trap-density model, a single trap density is instead set that is globally fitted. The bimolecular recombination rate constant is calculated based on instantaneous PL and THz measurements as before. The Auger recombination constant R_{Auger}, the de-trapping rate constant R_{detrap} and the depopulation rate R_{depop} are globally fitted at each temperature across three excitation fluences. The trap population rate is globally fitted across temperature and across fluence.

However, the assumption of a constant trap density is unable to reproduce the trends seen in the experiment, as shown in Figure S22. The measured PL transients show a fast initial decay that is followed by a very slow further decay. The fast initial component is slowing and the subsequent component accelerating with increasing temperature (Figure S22a). Furthermore, the magnitude of the initial decay tends to decrease with increasing temperature. This is reproduced nicely with a model that incorporates different trap densities above and below the phase transition (Figure S22b), but cannot be modelled if the trap density is assumed to be temperature independent (Figure S22c). The parameters resulting from fits assuming a constant trap density are shown in Figure S23.

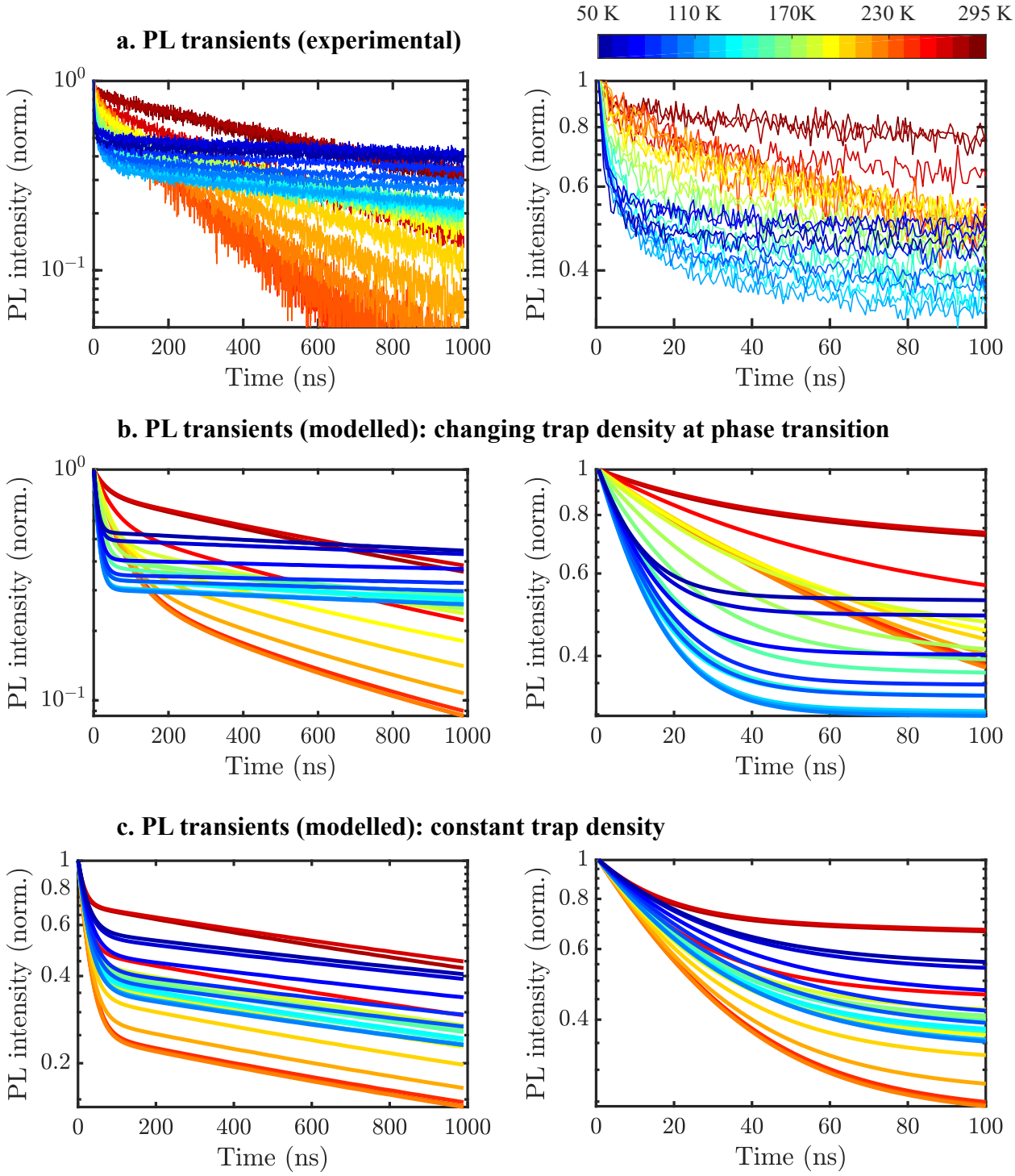

Figure S22: $FA_{0.95}Cs_{0.05}PbI_3$ thin film. Comparison of PL transient decays that are (a) experimentally measured, or modelled based on (b) the assumption of a different trap density in the high- and low-temperature phase or (c) a constant trap density at all temperatures. PL transients are shown from 50 K to 295 K at low excitation fluence (3.6 nJ/cm^2). The left-hand column column shows the PL transients up to 1000 ns, and the right-hand column up to 100 ns.

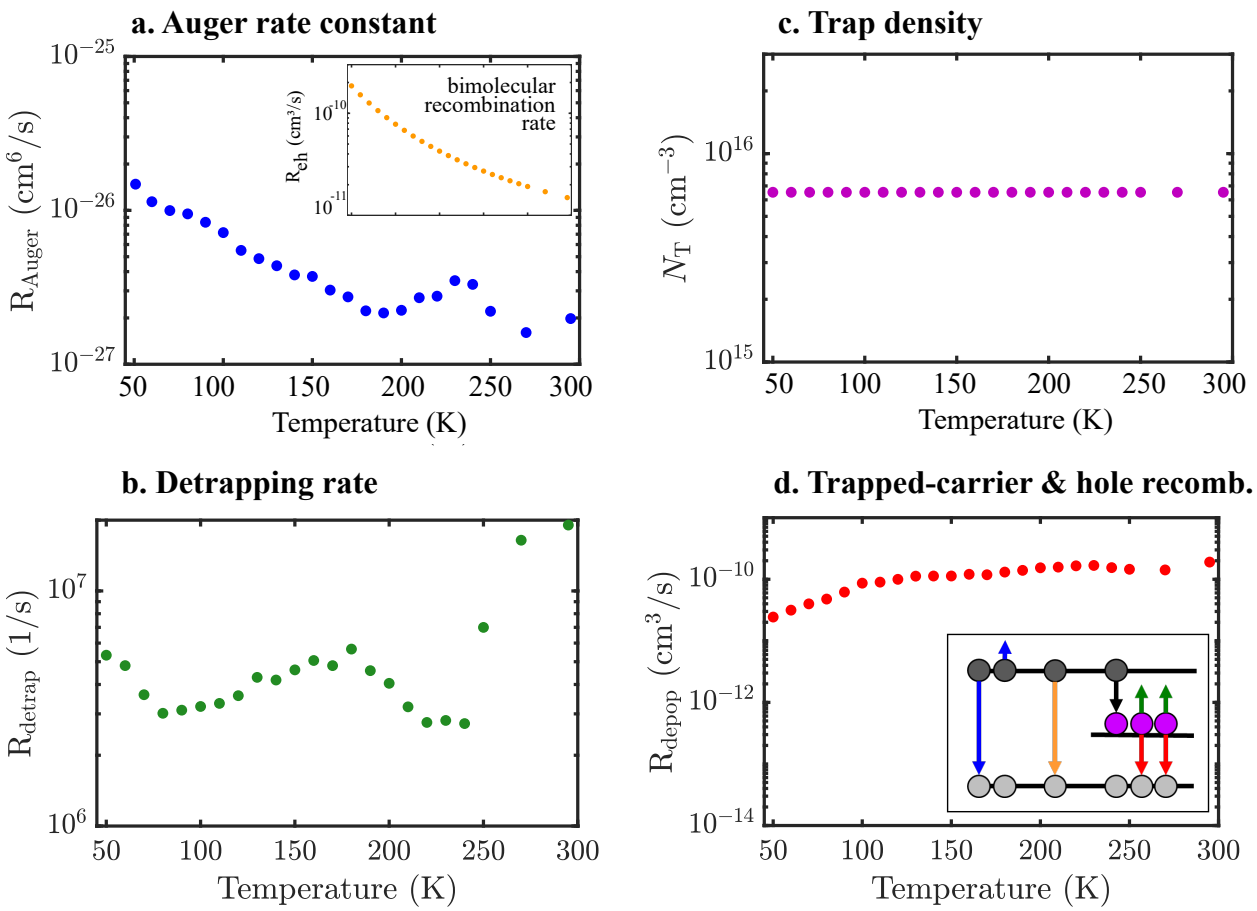

Figure S23: $FA_{0.95}Cs_{0.05}PbI_3$ thin film. Parameters extracted from analysis and fits of PL transients for a $FA_{0.95}Cs_{0.05}PbI_3$ thin film across temperatures between 50 K and 295 K and three excitation fluences, assuming a constant trap density. Parameters extracted from analysis and fits of PL transients for a $FA_{0.95}Cs_{0.05}PbI_3$ thin film across temperatures between 50 K and 295 K and three excitation fluences. The bimolecular recombination constant R_{eh} (inset in a) is determined from the instantaneous PL emission intensity, scaled by a room-temperature value extracted from THz photoconductivity transients. (a) The Auger recombination constant R_{Auger} and (b) the detrapping rate constant R_{detrap} are extracted from global fits to transients across three excitation fluences, at each given temperature. (c) The trap density N_T is determined from global fits to transients across three fluences and all temperature, and assumed to be temperature-independent. (d) The depopulation rate constant R_{depop} is extracted from global fits to transients across three excitation fluences, at each given temperature and represents the final recombination of trapped electrons with VB holes. A population constant $R_{pop} = 7.6 \times 10^{-9}\,\mathrm{cm}^3/\mathrm{s}$ is returned by global fits across all transients. The schematic model in inset (d) shows the different transitions in the colors corresponding to those used for the graphical display of the corresponding individual rate constants.

References

(S1) Lee, J. W.; Kim, D. H.; Kim, H. S.; Seo, S. W.; Cho, S. M.; Park, N. G. Formamidinium and cesium hybridization for photo- and moisture-stable perovskite solar cell. *Advanced Energy Materials* **2015**, *5*, 1501310.

(S2) Rehman, W.; McMeekin, D. P.; Patel, J. B.; Milot, R. L.; Johnston, M. B.; Snaith, H. J.; Herz, L. M. Photovoltaic mixed-cation lead mixed-halide perovskites: Links between crystallinity, photo-stability and electronic properties. *Energy and Environmental Science* **2017**, *10*, 361–369.

(S3) Saliba, M.; Matsui, T.; Seo, J. Y.; Domanski, K.; Correa-Baena, J. P.; Nazeeruddin, M. K.; Zakeeruddin, S. M.; Tress, W.; Abate, A.; Hagfeldt, A.; Grätzel, M. Cesium-containing triple cation perovskite solar cells: Improved stability, reproducibility and high efficiency. *Energy and Environmental Science* **2016**, *9*, 1989–1997.

(S4) Choi, H.; Jeong, J.; Kim, H. B.; Kim, S.; Walker, B.; Kim, G. H.; Kim, J. Y. Cesium-doped methylammonium lead iodide perovskite light absorber for hybrid solar cells. *Nano Energy* **2014**, *7*, 80–85.

(S5) Yi, C.; Luo, J.; Meloni, S.; Boziki, A.; Ashari-Astani, N.; Grätzel, C.; Zakeeruddin, S. M.; Röthlisberger, U.; Grätzel, M. Entropic stabilization of mixed A-cation ABX3 metal halide perovskites for high performance perovskite solar cells. *Energy and Environmental Science* **2016**, *9*, 656–662.

(S6) Burschka, J.; Pellet, N.; Moon, S. J.; Humphry-Baker, R.; Gao, P.; Nazeeruddin, M. K.; Grätzel, M. Sequential deposition as a route to high-performance perovskite-sensitized solar cells. *Nature* **2013**, *499*, 316–319.

(S7) Song, Z.; Watthage, S. C.; Phillips, A. B.; Tompkins, B. L.; Ellingson, R. J.; Heben, M. J. Impact of Processing Temperature and Composition on the Formation of Methylammonium Lead Iodide Perovskites. *Chem. Mater.* **2015**, *27*, 4612–4619.

(S8) Borchert, J.; Milot, R. L.; Patel, J. B.; Davies, C. L.; Wright, A. D.; Mart, L.; Snaith, H. J.; Herz, L. M.; Johnston, M. B. Large-Area, Highly Uniform Evaporated Formamidinium Lead Triiodide Thin Films for Solar Cells. *ACS Energy Letters* **2017**, *2*, 2799–2804.

(S9) Weller, M. T.; Weber, O. J.; Frost, J. M.; Walsh, A. Cubic Perovskite Structure of Black Formamidinium Lead Iodide, $\alpha[HC(NH_2)_2]PbI_3$, at 298 K. *Journal of Physical Chemistry Letters* **2015**, *6*, 3209–3212.

(S10) Xie, L. Q.; Chen, L.; Nan, Z. A.; Lin, H. X.; Wang, T.; Zhan, D. P.; Yan, J. W.; Mao, B. W.; Tian, Z. Q. Understanding the Cubic Phase Stabilization and Crystallization Kinetics in Mixed Cations and Halides Perovskite Single Crystals. *Journal of the American Chemical Society* **2017**, *139*, 3320–3323.

(S11) Fouladi, F.; Seyed, Y.; Kanjouri, F. Results in Physics MAPbI 3 and FAPbI 3 perovskites as solar cells : Case study on structural , electrical and optical properties. *Results in Physics* **2018**, *10*, 616–627.

(S12) Zhu, C.; Niu, X.; Fu, Y.; Li, N.; Hu, C.; Chen, Y.; He, X.; Na, G.; Liu, P.; Zai, H.; Ge, Y.; Lu, Y.; Ke, X.; Bai, Y.; Yang, S.; Chen, P.; Li, Y.; Sui, M.; Zhang, L.; Zhou, H.; Chen, Q. Strain engineering in perovskite solar cells and its impacts on carrier dynamics. *Nature Communications* **2019**, *10*, 815.

(S13) Wright, A. D.; Milot, R. L.; Eperon, G. E.; Snaith, H. J.; Johnston, M. B.; Herz, L. M. Band-Tail Recombination in Hybrid Lead Iodide Perovskite. *Advanced Functional Materials* **2017**, *27*, 1–8.

(S14) Wright, A. D.; Verdi, C.; Milot, R. L.; Eperon, G. E.; Pérez-Osorio, M. A.; Snaith, H. J.; Giustino, F.; Johnston, M. B.; Herz, L. M. Electron-phonon coupling in hybrid lead halide perovskites. *Nature Communications* **2016**, *7*, 11755.

(S15) Davies, C. L.; Borchert, J.; Xia, C. Q.; Milot, R. L.; Kraus, H.; Johnston, M. B.; Herz, L. M. Impact of the Organic Cation on the Optoelectronic Properties of Formamidinium Lead Triiodide. *The Journal of Physical Chemistry Letters* **2018**, *9*, 4502–4511.

(S16) Fabini, D. H.; Stoumpos, C. C.; Laurita, G.; Kaltzoglou, A.; Kontos, A. G.; Falaras, P.; Kanatzidis, M. G.; Seshadri, R. Reentrant Structural and Optical Properties and Large Positive Thermal Expansion in Perovskite Formamidinium Lead Iodide. *Angewandte Chemie - International Edition* **2016**, *55*, 15392–15396.

(S17) Chen, T.; Foley, B. J.; Park, C.; Brown, C. M.; Harriger, L. W.; Lee, J.; Ruff, J.; Yoon, M.; Choi, J. J.; Lee, S. H. Entropy-driven structural transition and kinetic trapping in formamidinium lead iodide perovskite. *Science Advances* **2016**, *2*, 10.

(S18) Jones, T. W.; Osherov, A.; Alsari, M.; Sponseller, M.; Duck, B. C.; Jung, Y.-K.; Settens, C.; Niroui, F.; Brenes, R.; Stan, C. V.; Li, Y.; Abdi-Jalebi, M.; Tamura, N.; Macdonald, J. E.; Burghammer, M.; Friend, R. H.; Bulovic, V.; Bulovic, B.; Walsh, A.; Wilson, G. J.; Lilliu, S.; Stranks, S. D. Lattice strain causes non-radiative losses in halide perovskites. *Energy Environ. Sci* **2019**, *12*, 596–606.

(S19) Wakahara, A.; Nomura, Y.; Ishii, M.; Kuramoto, K.; Sasaki, A. Strain effects on photoluminescence properties of Ge/Si disordered superlattices. *Journal of Applied Physics* **1997**, *81*, 7961–7965.

(S20) Yong, C. K.; Parkinson, P.; Kondratuk, D. V.; Chen, W. H.; Stannard, A.; Summerfield, A.; Sprafke, J. K.; O'Sullivan, M. C.; Beton, P. H.; Anderson, H. L.; Herz, L. M. Ultrafast delocalization of excitation in synthetic light-harvesting nanorings. *Chemical Science* **2015**, *6*, 181–189.

(S21) Kubin, R. Fluorescence quantum yields of some rhodamine dyes. *Journal of Luminescence* **1982**, *27*, 455–462.

(S22) Fischer, M.; Georges, J. Fluorescence quantum yield of rhodamine 6G in ethanol as a function of concentration using thermal lens spectrometry. **1996**, *260*, 115–118.

(S23) Penzkofer, A.; Lu, Y. Fluorescence quenching of rhodamine 6G in methanol at high concentration. *Chemical Physics* **1986**, *103*, 399–405.

(S24) Brenes, R.; Eames, C.; Bulović, V.; Islam, M. S.; Stranks, S. D. The Impact of Atmosphere on the Local Luminescence Properties of Metal Halide Perovskite Grains. *Advanced Materials* **2018**, *30*, 1706208.

(S25) Feng, X.; Su, H.; Wu, Y.; Wu, H.; Xie, J.; Liu, X.; Fan, J.; Dai, J.; He, Z. Photon-generated carriers excite superoxide species inducing long-term photoluminescence enhancement of $MAPbI_3$ perovskite single crystals. *Journal of Materials Chemistry A* **2017**, *5*, 12048–12053.

(S26) Tian, Y.; Peter, M.; Unger, E.; Abdellah, M.; Zheng, K.; Pullerits, T.; Yartsev, A.; Sundström, V.; Scheblykin, I. G. Mechanistic insights into perovskite photoluminescence enhancement: Light curing with oxygen can boost yield thousandfold. *Physical Chemistry Chemical Physics* **2015**, *17*, 24978–24987.

(S27) Motti, S. G.; Gandini, M.; Barker, A. J.; Ball, J. M.; Srimath Kandada, A. R.; Petrozza, A. Photoinduced Emissive Trap States in Lead Halide Perovskite Semiconductors. *ACS Energy Letters* **2016**, *1*, 726–730.

(S28) Crothers, T. W.; Milot, R. L.; Patel, J. B.; Parrott, E. S.; Schlipf, J.; Müller-Buschbaum, P.; Johnston, M. B.; Herz, L. M. Photon Reabsorption Masks Intrinsic Bimolecular Charge-Carrier Recombination in $CH_3NH_3PbI_3$ Perovskite. *Nano Letters* **2017**, *17*, 5782–5789.

(S29) Yamada, Y.; Yamada, T.; Phuong, L. Q.; Maruyama, N.; Nishimura, H.; Wakamiya, A.; Murata, Y.; Kanemitsu, Y. Dynamic Optical Properties of

$CH_3NH_3PbI_3$ Single Crystals as Revealed by One- and Two-Photon Excited Photoluminescence Measurements. *Journal of the American Chemical Society* **2015**, *137*, 10456–10459.

(S30) D'Innocenzo, V.; Grancini, G.; Alcocer, M. J. P.; Kandada, A. R. S.; Stranks, S. D.; Lee, M. M.; Lanzani, G.; Snaith, H. J.; Petrozza, A. Excitons versus free charges in organo-lead tri-halide perovskites. *Nature Communications* **2014**, *5*, 3586.

(S31) Lin, Q.; Armin, A.; Nagiri, R. C. R.; Burn, P. L.; Meredith, P. Electro-optics of perovskite solar cells. *Nature Photonics* **2015**, *9*, 106–112.

(S32) Wu, K.; Bera, A.; Ma, C.; Du, Y.; Yang, Y.; Li, L.; Wu, T. Temperature-dependent excitonic photoluminescence of hybrid organometal halide perovskite films. *Physical Chemistry Chemical Physics* **2014**, *16*, 22476–22481.

(S33) Savenije, T. J.; Ponseca, C. S.; Kunneman, L.; Abdellah, M.; Zheng, K.; Tian, Y.; Zhu, Q.; Canton, S. E.; Scheblykin, I. G.; Pullerits, T.; Yartsev, A.; Sundström, V. Thermally activated exciton dissociation and recombination control the carrier dynamics in organometal halide perovskite. *Journal of Physical Chemistry Letters* **2014**, *5*, 2189–2194.

(S34) Sarritzu, V.; Sestu, N.; Marongiu, D.; Chang, X.; Wang, Q.; Masi, S.; Colella, S.; Rizzo, A.; Gocalinska, A.; Pelucchi, E.; Mercuri, M. L.; Quochi, F.; Saba, M.; Mura, A.; Bongiovanni, G. Direct or Indirect Bandgap in Hybrid Lead Halide Perovskites? *Advanced Optical Materials* **2018**, *6*, 1701254.

(S35) Davies, C. L.; Filip, M. R.; Patel, J. B.; Crothers, T. W.; Verdi, C.; Wright, A. D.; Milot, R. L.; Giustino, F.; Johnston, M. B.; Herz, L. M. Bimolecular recombination in methylammonium lead triiodide perovskite is an inverse absorption process. *Nature Communications* **2018**, *9*, 293.

(S36) Won, R.; Leung, K.; Yeh, S.-c. A.; Fang, Q. Effects of incomplete decay in fluorescence lifetime estimation. *Biomedical Optics Express* **2011**, *2*, 2517–2531.